2004

A Steady-State Impedance Model for a PEMFC Cathode

Qingzhi Guo
University of South Carolina - Columbia

Ralph E. White
University of South Carolina - Columbia, white@cec.sc.edu

Publication Info

Published in *Journal of the Electrochemical Society*, Volume 151, Issue 4, 2004, pages E133-E149.

Guo, Q., & White, R. E. (2004). A Steady-State Impedance Model for a PEMFC Cathode. *Journal of The Electrochemical Society*, *151* (4), E188 – E149
Publisher's Version: http://dx.doi.org/10.1149/1.1648024

Journal of The Electrochemical Society, **151** (4) E133-E149 (2004)
0013-4651/2004/151(4)/E133/17/$7.00 © The Electrochemical Society, Inc.

A Steady-State Impedance Model for a PEMFC Cathode

Qingzhi Guo* and Ralph E. White,z**

Center for Electrochemical Engineering, Department of Chemical Engineering, University of South Carolina, Columbia, South Carolina 29208, USA

A model for the simulation of the steady-state impedance response of a polymer electrolyte membrane fuel cell (PEMFC) cathode is presented. The catalyst layer of the electrode is assumed to consist of many flooded spherical agglomerate particles surrounded by a small volume fraction of gas pores. Stefan-Maxwell equations are used to describe the multicomponent gas-phase transport occurring in both the gas diffusion layer and the catalyst layer of the electrode. Liquid-phase diffusion of O_2 is assumed to take place in the flooded agglomerate particles. Newman's porous electrode theory is applied to determine over-potential distributions.
 [DOI: 10.1149/1.1648024]

Manuscript submitted July 21, 2003; revised manuscript received October 5, 2003. Available electronically February 20, 2004.

In a commercial polymer electrolyte membrane fuel cell (PEMFC), air is likely to be the ultimate candidate gas for the cathode due to its much lower cost compared to pure O_2. However, for an air cathode, the mass-transport limitation in its gas diffusion layer (GDL) becomes more and more significant with the increase of operating current density. Knowledge of the mass-transport limitations in an air cathode is important to us because this electrode is the most important source of loss in an air/H_2 PEMFC.[1]

Two common models are available in the literature for the study of a PEMFC air cathode. They are the steady-state polarization model and the steady-state impedance model. Bernardi and Verbrugge[2] developed a steady-state polarization model for a PEMFC. In their model, multicomponent gas-phase transport was considered for the GDL of an air cathode, and ionic (proton) conduction as well as liquid-phase diffusion of O_2 was considered for the catalyst layer (CAL). They found that the gas-phase transport limitation in the cathode GDL caused a limiting current in the cell. In their work, the cathode CAL was assumed to be completely flooded. This assumption was also adopted by a later work of Springer *et al.*,[1] who carried out an extensive study of the influence on cell performance of the multicomponent gas transport in the GDL and the ionic conduction as well as the liquid-phase diffusion of O_2 in a flooded CAL of an air cathode. Even if a model with the flooded CAL assumption was generally able to explain the experimental data, the product of the diffusivity and the solubility of O_2 in the liquid phase was overestimated.[1] To explain this, Springer *et al.*[1] suggested the existence of O_2 diffusion along grain boundaries in the flooded CAL. Another explanation for their overestimation is the presence of gas pores in the cathode CAL. Consider that gas-phase O_2 transport is much faster than liquid-phase O_2 transport. Even if the volume fraction of gas pores in the cathode CAL is expected to be a small number under operating conditions, a CAL having gas pores can support a much higher operating current than a flooded CAL. Pisani *et al.*[3] modified Bernardi and Verbrugge's steady-state polarization model[2] and considered the coexistence of three phases, gas phase, liquid phase, and solid phase in the cathode CAL, where the solid phase was assumed to consist of many cylindrical particles extending from the GDL side to the polymer electrolyte membrane (PEM) side. Both the liquid-phase diffusion of O_2 inside the flooded cylindrical particles (radial direction) and the multicomponent gas-phase transport outside the flooded cylindrical particles (axial direction) were considered. Their modified model was used satisfactorily to fit the experimental steady-state polarization data found in the literature. In the steady-state polarization model of Jaouen *et al.*,[4] the existence of gas pores in the cathode CAL was also considered. In contrast to the work of Pisani *et al.*,[3] the solid phase of their cathode CAL was assumed to consist of many spherical agglomerate particles. The existence of a double Tafel slope on a steady-state polarization curve due to the transport limitation by either ionic conduction or liquid-phase diffusion of O_2 and the existence of a quadric Tafel slope due to a combined limitation by both processes were extensively investigated by Jaouen *et al.*[4]

Compared to the steady-state polarization experiment, the steady-state impedance experiment is more useful for the study of mass-transport limitations in a PEMFC.[5-7] After perturbing a cell from its steady-state operating condition by a small sinusoidal signal in the form of either cell potential or operating current over a wide range of frequency, all the processes occurring in the cell with different time constants are to be resolved on an impedance plot. Because the dominating process in a PEMFC often changes with the change of its steady-state operating condition, a better understanding of the transport limitations in the cell is possible from a series of impedance experiments carried out at different steady-state operating current densities. Springer *et al.*[6,7] developed a steady-state impedance model for an air cathode, where the multicomponent gas transport in the GDL and the liquid-phase diffusion of O_2 in a flooded CAL as well as the ionic conduction over there were taken into account. Due to the assumption of a flooded CAL in their work, the overestimation of the product of the diffusivity and the solubility of O_2 in the liquid phase was again not avoided.

The objective of this work is to extend Jaouen *et al.*'s work[4] to the development of a steady-state impedance model for an air cathode. Gas-phase transport is assumed to occur in both the GDL and the CAL (see Fig. 1). The cathode CAL is assumed to have many flooded agglomerate particles, inside which the O_2 reduction reaction takes place. Outside the flooded agglomerate particles are gas pores. Similar to Springer *et al.*'s[6] steady-state impedance model, liquid water transport is not considered in this work. Even if it is likely that with the increase of operating current density, the volume fraction of gas pores in either the GDL or the CAL decreases,[2,3] we expect that a constant value of this parameter is maintained during each steady-state impedance measurement.

Mathematical Model

Multicomponent gas transport.—The multicomponent gas transport in a porous media such as the GDL and the CAL of a PEMFC cathode is described by the Stefan-Maxwell equation[8]

$$\nabla \mathbf{x}_i = \sum_{j=1, j\neq i}^{n} \frac{1}{c_G D_{ij}} (x_i N_j - x_j N_i) \qquad [1]$$

where x_i is the mole fraction of gas component i, $\nabla \mathbf{x}_i$ is the gradient vector of x_i, n is the number of gas components, c_G is the total gas concentration, N_i is the flux of gas component i, and D_{ij} is the effective binary diffusion coefficient related to a free stream binary diffusion coefficient D_{ij}^0 by

$$D_{ij} = \varphi^{1+p} D_{ij}^0$$

* Electrochemical Society Student Member.
** Electrochemical Society Fellow.
z E-mail: white@engr.sc.edu

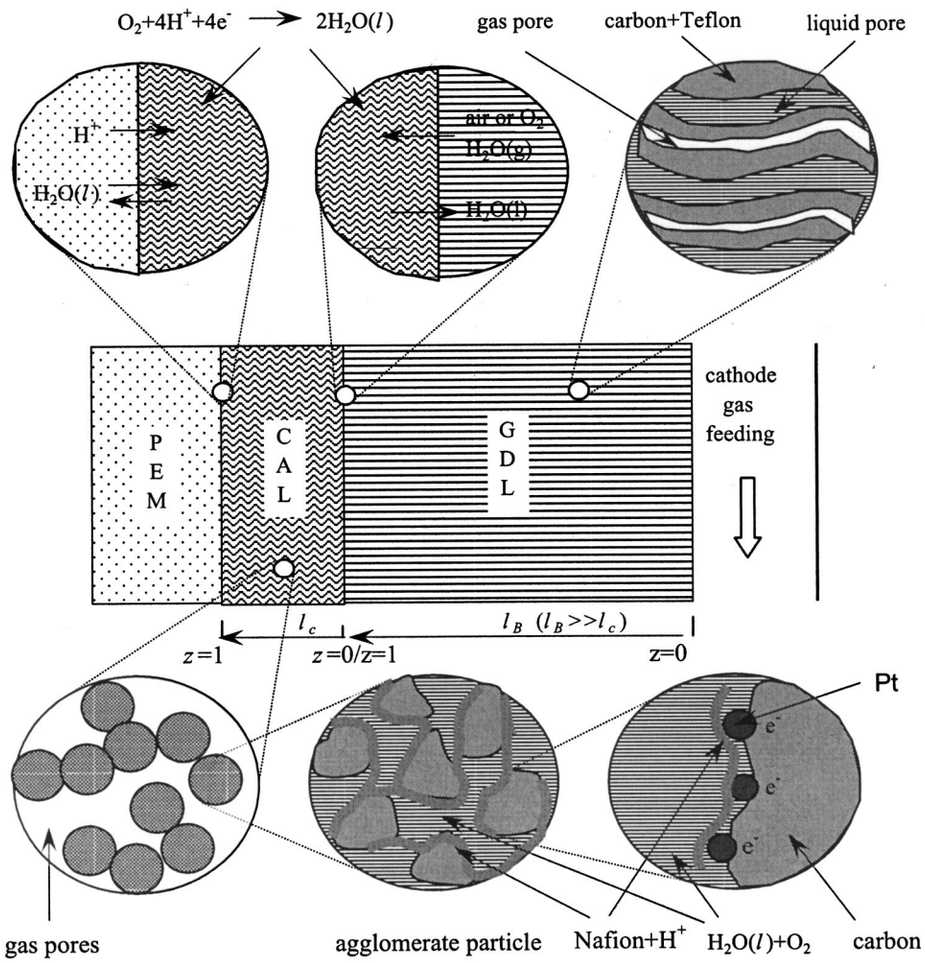

Figure 1. Illustration of the cathode for a polymer electrolyte membrane fuel cell.

where φ is the volume fraction of gas pores in the porous media, and *p* is the Bruggeman coefficient, assumed to be 0.5 throughout this work, to account for tortuosity effect.[1]

If a PEMFC and its two gas humidifiers are controlled at the same temperature, the isothermal and equilibrium water vapor saturation conditions are very likely to hold over the entire cell. If the gas pressures of a cell are well regulated, the isobaric condition is also valid in the gas pores of both the GDL and the CAL of the cathode. Unless it is mentioned otherwise, all the above conditions are assumed to be satisfied in this work, and the one-dimensional gas transport is considered to be valid (see Fig. 1).

For an O_2 cathode, only two components, O_2 and water vapor, exist in the gas phase of either the GDL or the CAL. Because a gas flow is always saturated by water vapor and the isobaric condition in the gas phase is maintained throughout, the partial pressure as well as the mole fraction of O_2 does not vary with time and spatial coordinate. In this case, the flux of gaseous O_2, N_O, is driven only by convection. The possible contribution to N_O from the diffusion mechanism disappears due to the absence of a concentration gradient of O_2. From Eq. 1, we find that there is a water vapor flux N_W dragged along with an O_2 flux

$$N_W = \frac{w}{1 - w} N_O \qquad [2]$$

where *w* is the mole fraction of water vapor. Equation 2 reveals that water vapor moves in the same direction as O_2. As a result, we can conclude that water is removed out of a PEMFC in the liquid form rather than in the vapor form. Moreover, the total amount of water to be removed out of a cell includes not only the amount produced by the O_2 reduction reaction assumed to follow a form

$$O_2 + 4H^+ + 4e^- \rightarrow 2H_2O(l) \qquad [3]$$

but also the amount of water vapor dragged along with the O_2 flux on the cathode side and the H_2 flux on the anode side. (Similar to Eq. 2, one can derive a flux of water vapor on the anode side.) This conclusion is also valid for an air cathode, which can be seen from the water vapor flux N_W given by Eq. 3 of Springer *et al.*'s work.[6]

For an air cathode, the gas phase is usually treated as a ternary system, and O_2, N_2, and H_2O have to be considered simultaneously in Eq. 1. A differential material balance on O_2 in the porous region i of the air cathode gives

$$c_G \varphi_i \frac{\partial x}{\partial t} = -\frac{1}{l_i} \frac{\partial N_O}{\partial z} + j_O \qquad [4]$$

where φ_i is the volume fraction of gas pores in the porous region i, *x* is the mole fraction of O_2, j_O is the accumulation rate of O_2 in the gas pores and equal to the molar rate of O_2 going to the gas pores from the flooded agglomerate particles per unit volume of the porous region i, and *z* is the spatial coordinate normalized by the thickness l_i of the porous region i.

A differential material balance on N_2 in the porous region i yields

$$c_G\varphi_i \frac{\partial y}{\partial t} = -\frac{1}{l_i}\frac{\partial N_N}{\partial z} \quad [5]$$

where y is the mole fraction of N_2 and N_N is its flux.

A summation of Eq. 4 and 5 yields

$$c_G\varphi_i \frac{\partial(x+y)}{\partial t} = c_G\varphi_i \frac{\partial(1-w)}{\partial t} = -\frac{1}{l_i}\frac{\partial(N_O+N_N)}{\partial z} + j_O \quad [6]$$

Under the assumption that the air flow in the porous region i of a cathode is always saturated by water vapor,[6] the value of w is fixed at all times and Eq. 6 is simplified to

$$\frac{\partial(N_O+N_N)}{\partial z} = j_O l_i \quad [7]$$

from which it is not difficult for one to conclude the existence of a uniform combined flux of O_2 and N_2 in the GDL where $j_O = 0$. If we assume that there is no flux of either O_2 or N_2 going to the PEM,[1,3,6] we can integrate Eq. 7 over the entire CAL where $j_O \neq 0$ and find the uniform combined flux of O_2 and N_2 in the GDL

$$N_O + N_N = -l_c\int_0^1 j_O dz \quad [8]$$

where the subscript c represents the CAL. Under a steady-state operation condition, we have

$$l_c\int_0^1 j_O dz = \frac{I}{4F} \quad [9]$$

where F is the Faradaic constant and I is the operating current density of a PEMFC. A negative sign is assigned to I in our model for the discharging process.

By using Eq. 1 and 8 and following a procedure similar to that explained in Springer *et al.*'s work,[6] we can find N_N in the GDL from

$$\frac{l_B}{\varphi_B^{1+p}D_{ON}^0 c_G}N_N = \frac{1}{\beta_1}\left[\frac{-l_c\int_0^1 j_O dz}{\varphi_B^{1+p}D_{ON}^0 c_G/l_B}(\beta_1 - x) + \frac{\beta_1+\beta_2 x}{\beta_3+\beta_2 x}\frac{\partial x}{\partial z}\right] \quad [10]$$

where the subscript B represents the GDL, $\beta_1 = 1 - w$, $\beta_2 = D_{WN}/D_{OW} - 1$, and $\beta_3 = 1 - w + wD_{ON}/D_{OW}$.

Equation 7 can be integrated from the GDL/CAL interface to any spatial coordinate z in the CAL to yield a combined flux of O_2 and N_2

$$N_O + N_N = -l_c\int_0^1 j_O dz + l_c\int_0^z j_O dz \quad [11]$$

which varies from $-l_c\int_0^1 j_O dz$ at $z = 0$ to zero at $z = 1$ in the CAL.

By using Eq. 1 and 11, we can find N_N in the CAL from

$$\frac{l_c}{\varphi_c^{1+p}D_{ON}^0 c_G}N_N = \frac{1}{\beta_1}\left[\frac{-l_c\int_0^1 j_O dz + l_c\int_0^z j_O dz}{\varphi_c^{1+p}D_{ON}^0 c_G/l_c}(\beta_1 - x) + \frac{\beta_1+\beta_2 x}{\beta_3+\beta_2 x}\frac{\partial x}{\partial z}\right] \quad [12]$$

Equations 8 and 10 to 12 are valid at all times. They are very useful for a dynamic model of an air cathode such as a steady-state impedance model.

Under a steady-state operating condition of a PEMFC, Eq. 5 yields a uniform N_N in the gas pores of the entire cathode. After applying an overall material balance on N_2 in the CAL, we find

$$N_N \equiv 0 \quad [13]$$

with which Eq. 10 is simplified to the first-order differential equation

$$\frac{\beta_1+\beta_2\bar{x}}{(\beta_1-\bar{x})(\beta_3+\beta_2\bar{x})}\frac{\partial\bar{x}}{\partial z} = \frac{I}{4F\varphi_B^{1+p}D_{ON}^0 c_G/l_B} \quad [14]$$

where an overbar is used for a variable to indicate a steady-state operating condition. Equation 14 can be used to find $\bar{x}$, the steady-state mole fraction of O_2, in the GDL at the steady-state operating current density $\bar{I}$.

After applying Eq. 13 to Eq. 12 for the CAL, we can obtain a simplified second-order differential equation

$$\frac{\beta_1+\beta_2\bar{x}}{(\beta_1-\bar{x})(\beta_3+\beta_2\bar{x})}\frac{\partial^2\bar{x}}{\partial z^2} + \frac{\beta_4+2\beta_1\beta_2\bar{x}+\beta_2^2\bar{x}^2}{(\beta_1-\bar{x})^2(\beta_3+\beta_2\bar{x})^2}\left(\frac{\partial\bar{x}}{\partial z}\right)^2 = \frac{-\bar{j}_O l_c}{\varphi_c^{1+p}D_{ON}^0 c_G/l_c} \quad [15]$$

where $\beta_4 = \beta_1\beta_3 - \beta_2\beta_1^2 + \beta_1\beta_2\beta_3$.

If the value of x at the GDL inlet is known, Eq. 14 can be integrated analytically to yield a solution of $\bar{x}$ in the GDL (see Eq. 5 of Ref. 6). To find $\bar{x}$ in the CAL from Eq. 15, we need two boundary conditions. One boundary condition can be specified by

$$\bar{x}|_{z=0,c} = \bar{x}|_{z=1,B} \quad [16]$$

to take advantage of the analytical solution of $\bar{x}$ in the GDL (Eq. 5 of Ref. 6). Another boundary condition can be found by considering zero flux of O_2 going to the PEM[1,3,6]

$$\left.\frac{\partial\bar{x}}{\partial z}\right|_{z=1,c} = 0 \quad [17]$$

After substituting Eq. 10 into Eq. 5 and applying $\partial y/\partial t = -\partial x/\partial t$, we have a differential equation that can be used to find the dynamic response of x in the GDL. During an impedance experiment on a PEMFC, a small sinusoidal signal in the form of either operating current or cell potential is usually applied to the cell under a steady-state operating condition. Due to the slight perturbation to the operating condition of the cell, linear responses are obtained. If any state variable, *i.e.*, x, in a dynamic model equation is written to be the sum of a steady-state term, $\bar{x}$, and a sinusoidal deviation term, $Re(\tilde{x}e^{j\omega t})$,[9] we can obtain a linear differential equation for the GDL in the frequency domain in terms of deviation variables such as $\tilde{x}$

$$\frac{\beta_1+\beta_2\bar{x}}{\beta_3+\beta_2\bar{x}}\frac{\partial^2\tilde{x}}{\partial z^2} + \left[2\frac{\beta_2(\beta_3-\beta_1)}{(\beta_3+\beta_2\bar{x})^2}\frac{\partial\bar{x}}{\partial z} + \frac{\bar{I}/4F}{\varphi_B^{1+p}D_{ON}^0 c_G/l_B}\right]\frac{\partial\tilde{x}}{\partial z} + \left[\frac{\beta_2(\beta_3-\beta_1)}{(\beta_3+\beta_2\bar{x})^2}\frac{\partial^2\bar{x}}{\partial z^2} - 2\left(\frac{\partial\bar{x}}{\partial z}\right)^2\frac{(\beta_3-\beta_1)\beta_2^2}{(\beta_3+\beta_2\bar{x})^3} - \frac{\beta_1\varphi_B j\omega}{\varphi_B^{1+p}D_{ON}^0/l_B^2}\right]\tilde{x} = -\frac{\partial\bar{x}}{\partial z}\frac{l_c\int_0^1\tilde{j}_O dz}{\varphi_B^{1+p}D_{ON}^0 c_G/l_B} \quad [18]$$

where a tilde is placed over a variable to indicate the deviation amplitude from a steady-state value of this variable. It is noted that all the deviation variables such as $\tilde{x}$ and $\tilde{j}_O$ are frequency-dependent complex variables.[9]

After substituting Eq. 12 into Eq. 5, we have a differential equation that can be used to find the dynamic response of x in the CAL. Similar to the procedure to get Eq. 18, we can obtain a differential equation for the CAL in the frequency domain

$$\frac{\beta_1+\beta_2\overline{x}}{\beta_3+\beta_2\overline{x}}\frac{\partial^2\tilde{x}}{\partial z^2}+\left[2\frac{\beta_2(\beta_3-\beta_1)}{(\beta_3+\beta_2\overline{x})^2}\frac{\partial\overline{x}}{\partial z}-\frac{-\overline{I}/4F+l_c\int_0^z\overline{j}_O dz}{\varphi_c^{1+p}D_{ON}^0c_G/l_c}\right]\times\frac{\partial\tilde{x}}{\partial z}+\left[-\frac{l_c\overline{j}_O}{\varphi_c^{1+p}D_{ON}^0c_G/l_c}+\frac{\beta_2(\beta_3-\beta_1)}{(\beta_3+\beta_2\overline{x})^2}\frac{\partial^2\overline{x}}{\partial z^2}-2\left(\frac{\partial\overline{x}}{\partial z}\right)^2\frac{(\beta_3-\beta_1)\beta_2^2}{(\beta_3+\beta_2\overline{x})^3}-\frac{\beta_1\varphi_c j\omega}{\varphi_c^{1+p}D_{ON}^0/l_c^2}\right]\tilde{x}+\frac{\beta_1-\overline{x}}{\varphi_c^{1+p}D_{ON}^0c_G/l_c}l_c\tilde{j}_O=\frac{\partial\overline{x}}{\partial z}\frac{-l_c\int_0^1\tilde{j}_O dz+l_c\int_0^z\tilde{j}_O dz}{\varphi_c^{1+p}D_{ON}^0c_G/l_c} \quad [19]$$

Three boundary conditions are required to solve Eq. 18 and 19. At the inlet of the GDL, we have $\tilde{x}=0$ obtained by assuming the existence of a fixed mole fraction of O_2 at the GDL inlet. At the CAL/PEM interface, we have $\partial\tilde{x}/\partial z=0$ due to zero flux of O_2 going to the PEM.[1,3,6] At the GDL/CAL interface, we have

$$\frac{\varphi_B^{1+p}}{l_B}\frac{\partial\tilde{x}}{\partial z}\bigg|_{z=1,B}=\frac{\varphi_c^{1+p}}{l_c}\frac{\partial\tilde{x}}{\partial z}\bigg|_{z=0,c} \quad [20]$$

which is obtained from the continuity of N_2 flux over there.

To summarize, Eq. 14 and 15 are used to find the steady-state $\overline{x}$ profiles in the GDL and the CAL, respectively, of an air cathode. These steady-state $\overline{x}$ profiles in the cathode are required by Eq. 18 and 19 to find $\tilde{x}$ profiles.

Overpotential distribution.—In the cathode CAL, gaseous O_2 has to dissolve in the liquid phase on the surface of a flooded spherical agglomerate particle before the O_2 reduction reaction takes place. The dissolved O_2 reacts on the catalyst sites along with its diffusion toward the center of an agglomerate particle.

A differential material balance on the dissolved O_2 in the liquid phase of an agglomerate particles gives[4]

$$\varepsilon\frac{\partial c}{\partial t}=\frac{\varepsilon^{1+p}D}{R^2}\frac{1}{r^2}\frac{\partial}{\partial r}\left(r^2\frac{\partial c}{\partial r}\right)-kc \quad [21]$$

where c is the concentration of the dissolved O_2, r is the radial coordinate normalized by the particle radius R_a, ε is the volume fraction of the liquid phase (including the hydrated Nafion ionomer) in the agglomerate particle, D is the diffusion coefficient of O_2 in a free liquid stream, and k is a reaction rate[4]

$$k=\frac{i_{ref}}{4Fc_{ref}}(1-\varepsilon)\exp\left(-\frac{\eta}{b}\right) \quad [22]$$

where i_{ref} is the exchange current density of the O_2 reduction reaction per unit volume of the Pt/carbon composite in the agglomerate particle at a reference O_2 concentration c_{ref}, b is the Tafel slope, and η is the overpotential of the agglomerate particle. It is assumed that η is uniform inside each agglomerate particle but varies with the spatial coordinate z.

One boundary condition can be specified for Eq. 21 by considering the existence of a symmetric c profile in a spherical agglomerate particle

$$\frac{\partial c}{\partial r}\bigg|_{r=0}=0 \quad [23]$$

Another boundary condition can be found by assuming that the concentration of the gaseous O_2 outside an agglomerate particle is always in equilibrium with the concentration of the dissolved O_2 on the agglomerate particle surface[4]

$$c|_{r=1}=c_G Hx \quad [24]$$

where H is Henry's constant.

Once the concentration profile of the dissolved O_2 inside an agglomerate particle is found, we can calculate $4Fj_e$, the reaction current per unit volume of the CAL, by integrating $-4Fkc$ over all the agglomerate particles per unit volume of the CAL

$$4Fi_e=-\frac{1-\varphi_c}{4\pi R_a^3/3}4\pi R_a^3\int_0^1 4Fkcr^2dr=-12F(1-\varphi_c)\int_0^1 kcr^2dr \quad [25]$$

where j_e is the molar rate of O_2 reacted per unit volume of the CAL. We can also calculate j_O by finding the flux of O_2 across all the surface area of agglomerate particles per unit volume of the CAL

$$j_O=\left(\frac{1-\varphi_c}{4\pi R_a^3/3}4\pi R_a^2\right)\left(-\frac{\varepsilon^{1+p}D}{R_a}\frac{\partial c}{\partial r}\bigg|_{r=1}\right)=-3(1-\varphi_c)\frac{\varepsilon^{1+p}}{R_a^2}\frac{\partial c}{\partial r}\bigg|_{r=1} \quad [26]$$

Under a steady-state operating condition, the time derivative term in Eq. 21 vanishes, and an analytical solution of $\overline{c}$ is available (see Appendix A). After applying the solution of $\overline{c}$ to Eq. 25 or 26, we can find

$$4F\overline{j}_e=4F\overline{j}_O=-12F(1-\varphi_c)\frac{\varepsilon^{1+p}D}{R_a^2}\times Hc_G\overline{x}\left[\sqrt{\frac{\overline{k}}{\frac{\varepsilon^{1+p}D}{R_a^2}}}\coth\left(\sqrt{\frac{\overline{k}}{\frac{\varepsilon^{1+p}D}{R_a^2}}}\right)-1\right] \quad [27]$$

where $\overline{k}$ is related to the steady-state overpotential $\overline{\eta}$ by

$$\overline{k}=\frac{i_{ref}}{4Fc_{ref}}(1-\varepsilon)\exp\left(-\frac{\overline{\eta}}{b}\right) \quad [28]$$

If we substitute $c=\overline{c}+Re(\tilde{c}e^{j\omega t})$, $x=\overline{x}+Re(\tilde{x}e^{j\omega t})$, and $\eta=\overline{\eta}+Re(\tilde{\eta}e^{j\omega t})$ into Eq. 21-24, we can obtain a differential equation in the frequency domain in terms of deviation variables

$$\frac{\varepsilon^{1+p}D}{R_a^2}\frac{1}{r^2}\frac{\partial}{\partial r}\left(r^2\frac{\partial\tilde{c}}{\partial r}\right)-(\overline{k}+j\varepsilon\omega)\tilde{c}+\overline{kc}\frac{\overline{\eta}}{b}=0 \quad [29]$$

subject to boundary conditions

$$\frac{\partial\tilde{c}}{\partial r}\bigg|_{r=0}=0 \quad [30]$$

$$\tilde{c}|_{r=1}=c_G H\overline{x} \quad [31]$$

An analytical solution of $\tilde{c}$ is available (see Appendix A), and we can obtain the deviation of the CAL reaction current, $4F\tilde{j}_e$, in the frequency domain

$$4F\tilde{j}_e = -12F(1-\varphi_c)\frac{\varepsilon^{1+P}D}{R_a^2}c_G H\bar{x}\times\left\{\frac{\sqrt{\frac{(\bar{k}+j\varepsilon\omega)}{\frac{\varepsilon^{1+P}D}{R_a^2}}}\coth\left(\sqrt{\frac{(\bar{k}+j\varepsilon\omega)}{\frac{\varepsilon^{1+P}D}{R_a^2}}}\right)-1}{1+j\frac{\varepsilon\omega}{\bar{k}}}\frac{\tilde{x}}{\bar{x}}\right.$$
$$\left.-\frac{\tilde{\eta}}{b}\frac{\frac{\sqrt{\frac{(\bar{k}+j\varepsilon\omega)}{\frac{\varepsilon^{1+P}D}{R_a^2}}}\coth\left(\sqrt{\frac{(\bar{k}+j\varepsilon\omega)}{\frac{\varepsilon^{1+P}D}{R_a^2}}}\right)-1}{1+j\frac{\varepsilon\omega}{\bar{k}}}-\left(1-j\frac{\varepsilon\omega}{\bar{k}}\right)\left[\sqrt{\frac{\bar{k}}{\frac{\varepsilon^{1+P}D}{R_a^2}}}\coth\left(\sqrt{\frac{\bar{k}}{\frac{\varepsilon^{1+P}D}{R_a^2}}}\coth\right)-1\right]}{j\frac{\varepsilon\omega}{\bar{k}}}\right\} \quad [32]$$

We can also obtain the deviation of the accumulation rate of O_2 in the gas phase, $\tilde{j}_O$, in the frequency domain

$$\bar{j}_O = -3(1-\varphi_c)\frac{\varepsilon^{1+P}D}{R_a{}^2}c_G H\bar{x}\times\left\{\left[\sqrt{\frac{(\bar{k}+j\varepsilon\omega)}{\frac{\varepsilon^{1+P}D}{R_a^2}}}\coth\left(\sqrt{\frac{(\bar{k}+j\varepsilon\omega)}{\frac{\varepsilon^{1+P}D}{R_a^2}}}\right)-1\right]\frac{\tilde{x}}{\bar{x}}\right.$$
$$\left.-\frac{\tilde{\eta}}{b}\frac{\sqrt{\frac{(\bar{k}+j\varepsilon\omega)}{\frac{\varepsilon^{1+P}D}{R_a^2}}}\coth\left(\sqrt{\frac{(\bar{k}+j\varepsilon\omega)}{\frac{\varepsilon^{1+P}D}{R_a^2}}}\right)-\sqrt{\frac{\bar{k}}{\frac{\varepsilon^{1+P}D}{R_a^2}}}\coth\left(\sqrt{\frac{\bar{k}}{\frac{\varepsilon^{1+P}D}{R_a^2}}}\right)}{j\frac{\varepsilon\omega}{\bar{k}}}\right\} \quad [33]$$

For an air cathode, Eq. 32 and 33 are both required for the calculation of impedance responses, while only Eq. 32 is necessary for an O_2 cathode. For an O_2 cathode, $\tilde{x}$ is equal to zero (x is uniform across the cathode). As a result, Eq. 32 can be further simplified to

$$4F\tilde{j}_e = 12F(1-\varphi_c)\frac{\varepsilon^{1+P}D}{R^2}c_G H\bar{x}$$
$$\times\left\{\frac{\frac{\sqrt{\frac{(\bar{k}+j\varepsilon\omega)}{\frac{\varepsilon^{1+P}D}{R_a^2}}}\coth\left(\sqrt{\frac{(\bar{k}+j\varepsilon\omega)}{\frac{\varepsilon^{1+P}D}{R_a^2}}}\right)-1}{1+j\frac{\varepsilon\omega}{\bar{k}}}-\left(1-j\frac{\varepsilon\omega}{\bar{k}}\right)\left[\sqrt{\frac{\bar{k}}{\frac{\varepsilon^{1+P}D}{R_a^2}}}\coth\left(\sqrt{\frac{\bar{k}}{\frac{\varepsilon^{1+P}D}{R_a^2}}}\right)-1\right]}{j\frac{\varepsilon\omega}{\bar{k}}}\right\} \quad [34]$$

In the above analysis, the liquid-phase diffusion of O_2 in a flooded agglomerate particle is modeled. The reaction currents, $4F\bar{j}_e$ and $4F\tilde{j}_e$, as well as the accumulation rates of O_2 in the gas phase, $\bar{j}_O$ and $\tilde{j}_O$, are solved analytically to be related to the local mole fractions of O_2, $\bar{x}$, and $\tilde{x}$, and to the local overpotentials, $\bar{\eta}$ and $\tilde{\eta}$, whose distributions are discussed as follows.

The modified Ohm's law for the polymer electrolyte, which is assumed to be present only within the agglomerate particles (see Fig. 1), of the CAL of an air cathode gives[10]

$$i_2 = -\frac{\kappa_{eff}}{l_c}\frac{\partial\Phi_2}{\partial z} + \frac{\kappa_{eff}RT}{4Fl_c}\frac{\partial \ln x}{\partial z} \quad [35]$$

where i_2 is the electrolyte current, Φ_2 is the electrolyte potential measured hypothetical reference O_2 laced right outside the surface of an agglomerate particle, R is the universal gas constant, T is the absolute temperature, and κ_{eff} is the effective ionic conductivity of the electrolyte.

The definition of the electrolyte potential Φ_2 by using a reference O_2 electrode allows U, the theoretical local equilibrium poten-

tial of a cathode measured with a reference O_2 electrode, to equal zero. The calculation of the cathode overpotential is then simplified to

$$\eta = \Phi_1 - \Phi_2 - U = \Phi_1 - \Phi_2 \quad [36]$$

where Φ_1 is the solid-phase potential assumed to be uniform in the CAL. The cathode potential in reference to a standard hydrogen electrode placed at the CAL/PEM interface can be calculated by

$$\Phi_1 = (E + \eta)|_{z=1,c} \quad [37]$$

where E is the equilibrium potential of the O_2 reference electrode in reference to a standard hydrogen electrode and can be calculated by the Nernst equation

$$E = E_O^0 + \frac{RT}{4F}\ln(Px) \quad [38]$$

where E_O^0 is the standard potential of the O_2 reference electrode in reference to a standard H_2 electrode and P is the total cathode gas pressure.

Conservation of charge in the CAL is governed by[11]

$$\frac{1}{l_c}\frac{\partial i_2}{\partial z} = 4Fj_e + (1-\varphi_c)(1-\varepsilon)C_{dl}\frac{\partial \eta}{\partial t} \quad [39]$$

where C_{dl} is the double-layer capacitance per unit volume of the Pt/carbon composite. Both the catalyst Pt and its carbon support are supposed to contribute to C_{dl}.

A combination of Eq. 35, 36, and 39 yields

$$\frac{\partial^2 \eta}{\partial z^2} = \frac{l_c}{\kappa_{eff}}\left[4Fj_e l_c + (1-\varphi_c)(1-\varepsilon)C_{dl}l_c\frac{\partial \eta}{\partial t}\right] - \frac{RT}{4F}\frac{\partial^2 \ln x}{\partial z^2} \quad [40]$$

subject to boundary conditions

$$\left.\frac{\partial \eta}{\partial z}\right|_{z=0,c} = -\left.\frac{RT}{4F}\frac{\partial \ln x}{\partial z}\right|_{z=0,c} \quad [41]$$

and

$$\left.\frac{\partial \eta}{\partial z}\right|_{z=1,c} = \frac{l_c}{\kappa_{eff}} I \quad [42]$$

where zero O_2 gas flux going to the PEM is implicitly applied.

Equations 40-42 are valid for an air cathode at all times. Under a steady-state operating condition, no current goes to double-layer charging and Eq. 40 is simplified to

$$\frac{\partial^2 \overline{\eta}}{\partial z^2} = \frac{l_c}{\kappa_{eff}} 4F\overline{j_e} l_c - \frac{RT}{4F}\frac{\partial^2 \ln \overline{x}}{\partial z^2} \quad [43]$$

subject to the boundary conditions similar to Eq. 41 and 42 except that η is replaced by $\overline{\eta}$, x is replaced by $\overline{x}$ and I is replaced by $\overline{I}$.

The substitution of $\eta = \overline{\eta} + \mathrm{Re}(\tilde{\eta}e^{j\omega t})$, $j_e = \overline{j_e} + \mathrm{Re}(\tilde{j}_e e^{j\omega t})$ and $x = \overline{x} + \mathrm{Re}(\tilde{x}e^{j\omega t})$ into Eq. 40 yields a differential equation in the frequency domain in terms of deviation variables

$$\frac{\partial^2 \tilde{\eta}}{\partial z^2} = \frac{l_c}{\kappa_{eff}}[4F\tilde{j}_e l_c + j\omega(1-\varphi_c)(1-\varepsilon)C_{dl}l_c\tilde{\eta}] - \frac{RT}{4F}\frac{\partial^2\left(\frac{\tilde{x}}{\overline{x}}\right)}{\partial z^2} \quad [44]$$

subject to boundary conditions

$$\left.\frac{\partial \tilde{\eta}}{\partial z}\right|_{z=0,c} = -\left.\frac{RT}{4F}\frac{\partial\left(\frac{\tilde{x}}{\overline{x}}\right)}{\partial z}\right|_{z=0,c} \quad [45]$$

and

$$\left.\frac{\partial \tilde{\eta}}{\partial z}\right|_{z=1,c} = \frac{l_c}{\kappa_{eff}}\tilde{I} \quad [46]$$

For an O_2 cathode, neither $\overline{x}$ nor $\tilde{x}$ is the variable to be solved for. Therefore, Eq. 43 to 45 can be simplified to

$$\frac{\partial^2 \overline{\eta}}{\partial z^2} = \frac{l_c}{\kappa_{eff}} 4F\overline{j_e} l_c \quad [47]$$

$$\frac{\partial^2 \tilde{\eta}}{\partial z^2} = \frac{l_c}{\kappa_{eff}}[4F\tilde{j}_e l_c + j\omega(1-\varphi_c)(1-\varepsilon)C_{dl}l_c\tilde{\eta}] \quad [48]$$

$$\left.\frac{\partial \tilde{\eta}}{\partial z}\right|_{z=0,c} = 0 \quad [49]$$

The impedance response Z of an air cathode under a steady-state operating condition can be calculated by finding the transfer function

$$Z = \frac{\tilde{\Phi}_1|_{z=1,c}}{\tilde{I}} = \frac{(\tilde{E}+\tilde{\eta})|_{z=1,c}}{\tilde{I}} = \frac{\left.\left(\frac{RT}{4F}\frac{\tilde{x}}{\overline{x}} + \tilde{\eta}\right)\right|_{z=1,c}}{\tilde{I}} \quad [50]$$

For convenience, we set $\tilde{I}$ to be unity in our impedance calculation. Then, Eq. 50 is simplified to

$$Z = \tilde{\Phi}_1|_{z=1,c} = \left.\left(\frac{RT}{4F}\frac{\tilde{x}}{\overline{x}} + \tilde{\eta}\right)\right|_{z=1,c} \quad [51]$$

For an O_2 cathode, the impedance response at a steady-state operating condition can be calculated by

$$Z = \tilde{\Phi}_1|_{z=1,c} = \tilde{\eta}|_{z=1,c} \quad [52]$$

Numerical solution.—The calculation of the impedance response of a PEMFC cathode under a steady-state operating condition requires the knowledge of steady-state profiles of the variables of interest. Therefore, these profiles are also part of our calculation in order to obtain the steady-state impedance response of a cathode.

For a differential equation such as Eq. 18 involving some complex variables, even if its numerical solution can be handled in the complex domain by some numerical solvers, our available solver only allows its numerical solution in the real domain. Therefore, Eq. 18 has to be split into two equations[9]

$$\frac{\beta_1 + \beta_2\overline{x}}{\beta_3 + \beta_2\overline{x}}\frac{\partial^2 \tilde{x}_{Re}}{\partial z^2} + \left[2\frac{\beta_2(\beta_3-\beta_1)}{(\beta_3+\beta_2\overline{x})^2}\frac{\partial \overline{x}}{\partial z} + \frac{\overline{I}/4F}{{\varphi_B}^{1+p}D_{ON}^0 c_G/l_B}\right] \times \frac{\partial \tilde{x}_{Re}}{\partial z} + \left[\frac{\beta_2(\beta_3-\beta_1)}{(\beta_3+\beta_2\overline{x})^2}\frac{\partial^2 \overline{x}}{\partial z^2} - 2\left(\frac{\partial \overline{x}}{\partial z}\right)^2\frac{(\beta_3-\beta_1){\beta_2}^2}{(\beta_3+\beta_2\overline{x})^3}\right]\tilde{x}_{Re} + \frac{\beta_1\varphi_B\omega}{{\varphi_B}^{1+p}D_{ON}^0/{l_B}^2}\tilde{x}_{Im} = -\frac{\partial \overline{x}}{\partial z}\frac{l_c\int_0^1 \tilde{j}_{O,Re}dz}{{\varphi_B}^{1+p}D_{ON}^0 c_G/l_B} \quad [53]$$

and

Table I. Parameters used for the impedance simulation of a PEMFC cathode operated at 70°C.

	GDL	Catalyst layer	Comments
D^0_{ON}	0.230 cm^2/s	0.230 cm^2/s	Ref. 14 (T = 316 K, P = 1 atm)
D^0_{OW}	0.282 cm^2/s	0.282 cm^2/s	Ref. 14 (T = 308 K, P = 1 atm)
D^0_{NW}	0.293 cm^2/s	0.293 cm^2/s	Ref. 14 (T = 298 K, P = 1 atm)
l_B	0.04 cm		Measured on ELATs
φ_B	0.36		Assumed[1,4,6]
p	0.5	0.5	Ref. 1
φ_c		0.1	Assumed[3-4]
l_c		0.003 cm	Measured on ELATs
l_c/κ_{eff}		0.318 Ω cm^2	Assumed[1,4,6]
$i_{ref}/(4Fc_{ref})$		0.0015 s^{-1}	Assumed in this work
ε		0.5	Assumed[3,4]
C_{dl}		30 F/cm^3	Ref. 6
b		0.0261 V	Assumed[1,6]
D		6.22×10^{-6} cm^2/s	Ref. 15
H		0.0277 $[mol/cm^3(l)]/[mol/cm^3(g)]$	Ref. 15
R_a		1.0×10^{-4} cm	Assumed[4]
E^0_O		1.20 V	Ref. 15

[a] $D^0_{ij}(T,P) = D^0_{ij}(T_1,P_1) \times \frac{P_1}{P} \times \left(\frac{T}{T_1}\right)^{1.8}$

$$\frac{\beta_1 + \beta_2\overline{x}}{\beta_3 + \beta_2\overline{x}}\frac{\partial^2\tilde{x}_{Im}}{\partial z^2} + \left[2\frac{\beta_2(\beta_3 - \beta_1)}{(\beta_3 + \beta_2\overline{x})^2}\frac{\partial\overline{x}}{\partial z} + \frac{\overline{I}/4F}{{\varphi_B}^{1+p}D^0_{ON}c_G/l_B}\right] \times \frac{\partial\tilde{x}_{Im}}{\partial z} + \left[\frac{\beta_2(\beta_3 - \beta_1)}{(\beta_3 + \beta_2\overline{x})^2}\frac{\partial^2\overline{x}}{\partial z^2} - 2\left(\frac{\partial\overline{x}}{\partial z}\right)^2\frac{(\beta_3 - \beta_1){\beta_2}^2}{(\beta_3 + \beta_2\overline{x})^3}\right]\tilde{x}_{Im} - \frac{\beta_1\varphi_B\omega}{{\varphi_B}^{1+p}D^0_{ON}/{l_B}^2}\tilde{x}_{Re} = -\frac{\partial\overline{x}}{\partial z}\frac{l_c\int_0^1\tilde{j}_{O,Im}dz}{{\varphi_B}^{1+p}D^0_{ON}c_G/l_B} \quad [54]$$

where the subscripts Re and Im represent the real part and the imaginary part of a complex variable, respectively. A list of all the final equations such as Eq. 53 and 54 to be solved for the steady-state impedance response of a cathode are summarized in Appendix B, where the expressions for $\tilde{j}_{O,Re}$, $\tilde{j}_{O,Im}$, 4 $F\tilde{j}_{e,Re}$ and 4 $F\tilde{j}_{e,Im}$ in terms of other deviation variables such as $\tilde{x}_{Re}$, $\tilde{x}_{Re}$, $\tilde{\eta}_{Re}$, and $\tilde{\eta}_{Im}$ are available in Appendix C.

A three-point finite difference method is used to approximate the derivative of each variable in our model equations, a Trapezoidal's rule[12] is used to integrate a variable, and a general nonlinear equation solver in FORTRAN called GNES is used in our numerical calculation.[10] It is noted that even if a banded jacobian matrix is available for the calculation of the steady-state impedance response of an O_2 cathode, it is not available for the calculation of the impedance response of an air cathode due to the integration terms such as those in Eq. 53 and 54.

Results and Discussion

Parameter values.—It is assumed that the PEMFC under study here is operated at a cell temperature of 70°C. The base values for all the parameters used in the model are presented in Table I. Some of them were directly taken from the literature,[1,6,14,15] some of them were measured, and some of them were assumed. The assumed value for a parameter is obtained from the trade-off of different values used in the literature. For example, the volume fraction of gas pores in the CAL, φ_c, was assigned to a value of 0.3 in Ref. 4, while three different values, 0.01, 0.011, and 0.02, were used in Ref. 3. In this work, a value of 0.1 is assumed for this parameter.

Simulation results.—Due to the fact that the steady-state profiles of the variables of interest such as $\overline{x}$ and $\overline{\eta}$ are part of the calculation of the steady-state impedance response of a PEMFC cathode, both the steady-state polarization data and the steady-state impedance response can be predicted by the steady-state impedance model considered in this work. Figure 2a shows the simulated polarization curves of a PEMFC cathode operated under different gas pressures. One may observe that for an air cathode, each polarization curve displays a limiting current when the electrode potential goes below 0.4 V. The increase of the limiting current with the increase of gas pressure can be explained by an increase of the mole fraction of O_2 at the GDL inlet. One may also observe that the limiting currents predicted in this work are much higher than those reported in the literature.[1,3] However, these values are observable in a laboratory on a PEMFC with up-to-date technologies. On the polarization curve of a cathode with an air pressure of 1.0 atm, four places are marked by the plus signs, where the steady-state impedance responses are to be calculated and compared later. For the air cathode, the mole fractions of gaseous O_2 at the CALPEM interface are also calculated with the change of the steady-state operating current density and these results are presented in Fig. 2b. A comparison between these two figures shows that a limiting current appears when the mole fraction of gaseous O_2 drops to a negligible value. Therefore, the mass-transport limitation in the gas pores of an air cathode is responsible for the appearance of a limiting current.[1,2]

Throughout this work, each steady-state impedance plot is presented in a normalized form. Both the real part and the imaginary part of the impedance response are multiplied by the ratio of $-\overline{I}$, the steady-state operating current density, to b, the normal Tafel slope, to yield a normalized impedance response. With this kind of representation, the width of an impedance plot (on the real axis) is directly related to the apparent Tafel slope observed on a steady-state polarization curve, $\overline{\Phi}_1|_{z=1,c}$ *vs.* $\ln(-\overline{I})$, at the same steady-state operating current density. For example, if the width of a steady-state impedance plot reads 2, a double Tafel slope is shown on a polarization curve.

Under the ambient gas pressure, the impedance responses of a PEMFC air cathode are simulated for different steady-state operating current densities by this model (also called the full model below), and they are plotted in Fig. 3. In general, this model predicts an increase of the apparent Tafel slope with the increase of the steady-state operating current density. When a steady-state operating condition is close to open-circuit, only one impedance loop is observed and the apparent Tafel slope does not deviate much from the normal value, b. When a steady-state operating condition is away

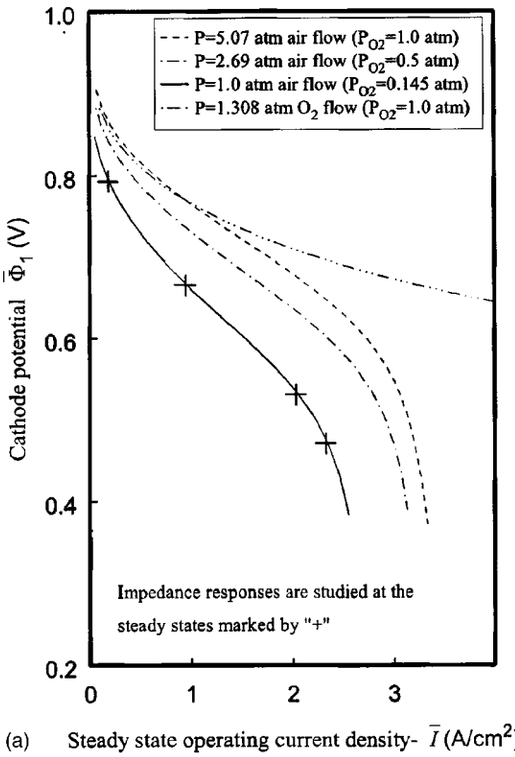

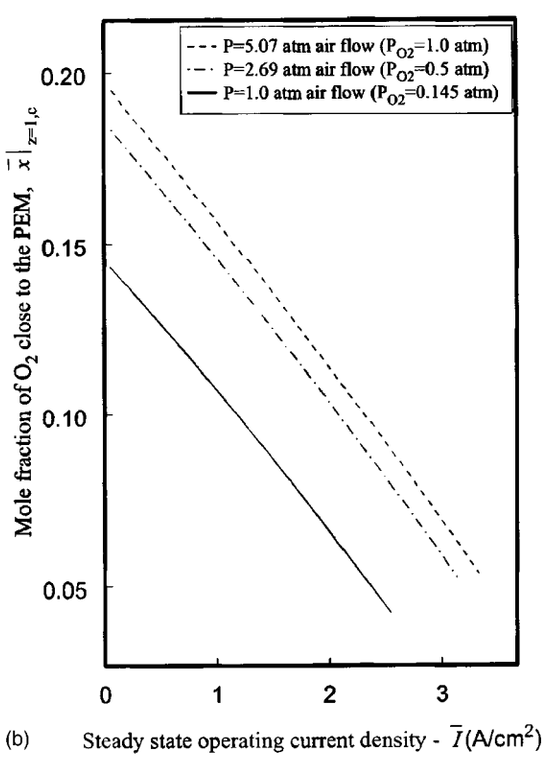

Figure 2. (a) Simulated steady-state polarization curves of a PEMFC cathode. The base value in Table I is assigned to each parameter in the model. (b) Simulated steady-state mole fractions of O_2 at the CAL/PEM interface of a PEMFC air cathode with the change of the operating current density. The base value in Table I is assigned to each parameter in the model.

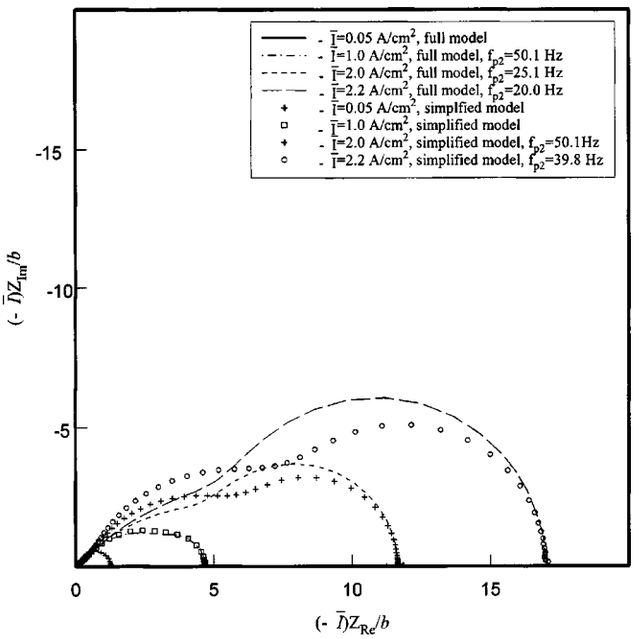

Figure 3. Comparison of the normalized impedance responses of a PEMFC air cathode operated under the ambient gas pressure between the full model and the simplified model.

from open-circuit, a second impedance loop appears and the apparent Tafel slope is larger than *b*. A limiting current is obtained when the second impedance loop becomes much bigger than the first one and when the apparent Tafel slope is infinitely large. Springer *et al.*[6] attributed the first impedance loop to the effective charge-transfer resistance and double-layer charging and the second one to the mass-transport limitation in the gas phase. They explained that the effective charge-transfer resistance was influenced not only by the interfacial O_2 reduction reaction but also by ionic conduction and liquid-phase O_2 diffusion.

The steady-state impedance model developed in this work is largely motivated by a pioneering work of Springer *et al.*[6] Unfortunately, there was an error associated with multicomponent gas transport in their work. This error was caused by their equating the uniform combined flux of O_2 and N_2 in the GDL to $-I/(4F)$ instead of the O_2 flux at the GDLCAL interface,[7] which indicated that the current for double-layer charging and liquid-phase O_2 storage was able to contribute to the combined flux of O_2 and N_2. Obviously, that is not true. To demonstrate the calculation accuracy of the impedance responses with such an error, a simplified model is developed from our full model by assuming

$$4Fj_O = \frac{1}{l_c}\frac{\partial i_2}{\partial z} = 4Fj_e + (1 - \varphi_c)(1 - \varepsilon)C_{dl}\frac{\partial \eta}{\partial t} \quad [55]$$

and the calculated impedance responses are also presented in Fig. 3. If the simplified model can predict the steady-state impedance responses of an air cathode within an acceptable error, the integration terms in our full-model equations can be avoided (see Eq. 53 and 54) and a banded jacobian matrix can be used to allow much faster numerical calculations. It is seen from Fig. 3 that at high steady-state current densities, even if the impedance responses calculated by both models agree in the very high and very low frequency limits, the simplified model overestimated the impedance responses in most of the high frequency region (high frequency loops) and underestimated those in most of the low frequency region (low frequency loops). To understand this, we consider a simple air cathode with an ultrathin CAL. In this case, the CAL behaves like a thin-film

diffusion electrode, and the distributions of overpotentials and mole fractions of O_2 in the CAL can be neglected. The normalized impedance response of this air cathode can be calculated by

$$\left(\frac{-\overline{I}}{b}\right)Z = \left(\frac{-\overline{I}}{b}\right)\frac{\tilde{\eta} + \tilde{E}}{\tilde{I}} = \left(\frac{-\overline{I}}{b}\right) \times\left[\frac{\tilde{\eta}}{4F\tilde{j}_e l_c + j\omega(1-\varphi_c)(1-\varepsilon)C_{dl}l_c\tilde{\eta}} + \frac{RT}{4F}\frac{\tilde{x}}{\overline{x}\tilde{I}}\right] \quad [56]$$

If the dissolved O_2 storage in the flooded agglomerate particles is neglected, either Eq. 32 or Eq. 33 yields

$$4F\tilde{j}_e l_c = 4F\tilde{j}_O l_c = \tilde{\eta}\left(\frac{-\overline{I}}{b}\right)\left(\frac{1}{k_1} - \frac{\tilde{x}/(\tilde{I}\overline{x})}{\tilde{\eta}/(\tilde{I}b)}\right) \quad [57]$$

where

$$k_1 = \frac{2[\sqrt{k'}\coth(\sqrt{k'}) - 1]}{\sqrt{k'}\coth(\sqrt{k'}) + k' - k'\coth(\sqrt{k'})^2},$$

$$k' = \overline{k}/\left(\frac{\varepsilon^{1+p}D}{R_a^{\,2}}\right), \text{ and } \overline{I} = 4F\overline{j}_e l_c \quad [58]$$

where k_1 ranges from 1 to 2 and reflects the change of the apparent Tafel slope with the change of the steady-state operating condition for a single agglomerate particle cathode. Equations 56 and 57 can be combined to yield

$$\left(\frac{-\overline{I}}{b}\right)Z = \frac{1}{\left(\frac{1}{k_1} - \frac{\tilde{x}/(\tilde{I}\overline{x})}{\tilde{\eta}/(\tilde{I}b)}\right) + \frac{j\omega(1-\varphi_c)(1-\varepsilon)C_{dl}l_c}{-\overline{I}/b} + \left(\frac{-\overline{I}}{b}\right)\frac{RT}{4F}\frac{\tilde{x}}{\overline{x}\tilde{I}}} \quad [59]$$

In the high-frequency region, we expect that the majority of the perturbation current goes to double-layer charging and $\tilde{x}$, the deviation of mole fraction of O_2, has a much smaller amplitude at the same frequency than that predicted from the simplified model, where all the perturbation current is assumed to influence $\tilde{x}$. It is not difficult for one to conclude from Eq. 59 that the overestimation of $\tilde{x}$ in the high-frequency region by the simplified model leads to a high estimation of Z. An explanation for the underestimation of Z in the low-frequency region by the simplified model is offered later.

The failure of the simplified model to predict accurately the impedance responses of a cathode motivates our interest in finding out how the total accumulation current of O_2 in the gas-phase changes, subject to the current perturbation, with frequency. Figure 4 shows the plots of $(4Fl_c\int_0^1\tilde{j}_O dz)/\tilde{I}$, the transfer function for the deviation of the total accumulation current of O_2 in the gas phase. Interestingly, this figure displays a transfer function profile similar to an impedance plot in Fig. 3. When the steady-state operating current density is small, *i.e.*, $-\overline{I} = 0.05$ A/cm^2, the transfer function profile has an almost exact semicircular shape. When the steady-state current density becomes high, two loops are displayed. These transfer function profiles can be understood by considering a similar air cathode with an ultrathin CAL (the dissolved O_2 storage in the flooded agglomerate particles is again neglected)

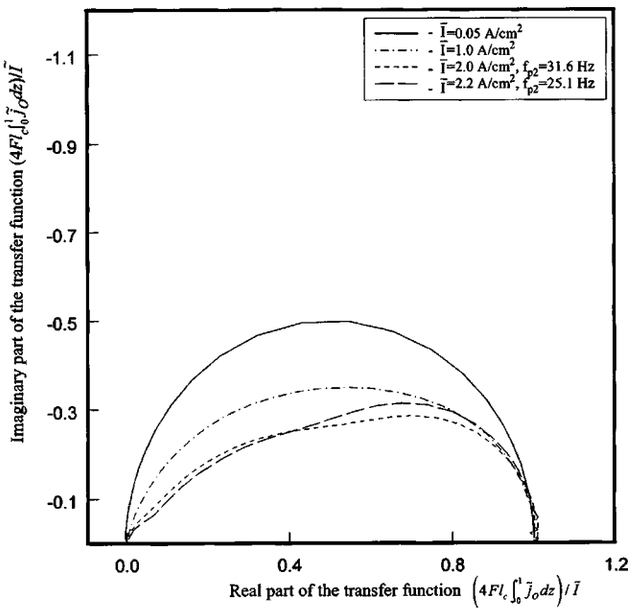

Figure 4. Transfer function for the deviation of the accumulation current of O_2, $(4Fl_c\int_0^1\tilde{j}_O dz)/\tilde{I}$, in the gas phase of a PEMFC air cathode under the ambient gas pressure.

$$\frac{Fl_c\int_0^1\tilde{j}_O dz}{\tilde{I}} = \frac{\tilde{I} - j\omega(1-\varphi_c)(1-\varepsilon)C_{dl}l_c\tilde{\eta}}{\tilde{I}} = 1 - \frac{j\omega(1-\varphi_c)(1-\varepsilon)C_{dl}l_c}{\left(\frac{-\overline{I}}{b}\right)\left(\frac{1}{k_1} - \frac{\tilde{x}/(\tilde{I}\overline{x})}{\tilde{\eta}/(\tilde{I}b)}\right) + j\omega(1-\varphi_c)(1-\varepsilon)C_{dl}l_c} \quad [60]$$

At a small steady-state operating current density, due to the relative importance of the sluggish charge-transfer reaction, $\tilde{\eta}/(\tilde{I}b)$ is much larger than $\tilde{x}/(\tilde{I}\overline{x})$, and consequently Eq. 60 is simplified to

$$\frac{4Fl_c\int_0^1\tilde{j}_O dz}{\tilde{I}} = 1 - \frac{j\omega(1-\varphi_c)(1-\varepsilon)C_{dl}l_c}{\left(\frac{-\overline{I}}{b}\right)\frac{1}{k_1} + j\omega(1-\varphi_c)(1-\varepsilon)C_{dl}l_c} \quad [61]$$

which predicts an exact semicircular profile whose width equals unity. At a high steady-state operating current density, $\tilde{x}/(\tilde{I}\overline{x})$ becomes comparable to $\tilde{\eta}/(\tilde{I}b)$ in the low frequency region due to a reduced value of x ($\tilde{x}$ does not change much with the change of the steady-state operating current density, as is justified later) and a reduced value of $\tilde{\eta}/\tilde{I}$, and consequently the mass-transport limitation of O_2 in the gas pores is reflected on a transfer function profile by displaying a low-frequency loop. One may notice that the peak frequencies for the second loop are slightly larger than those in Fig. 3. An explanation is that the impedance response of an air cathode is calculated at the CAL/PEM interface, but the transfer function

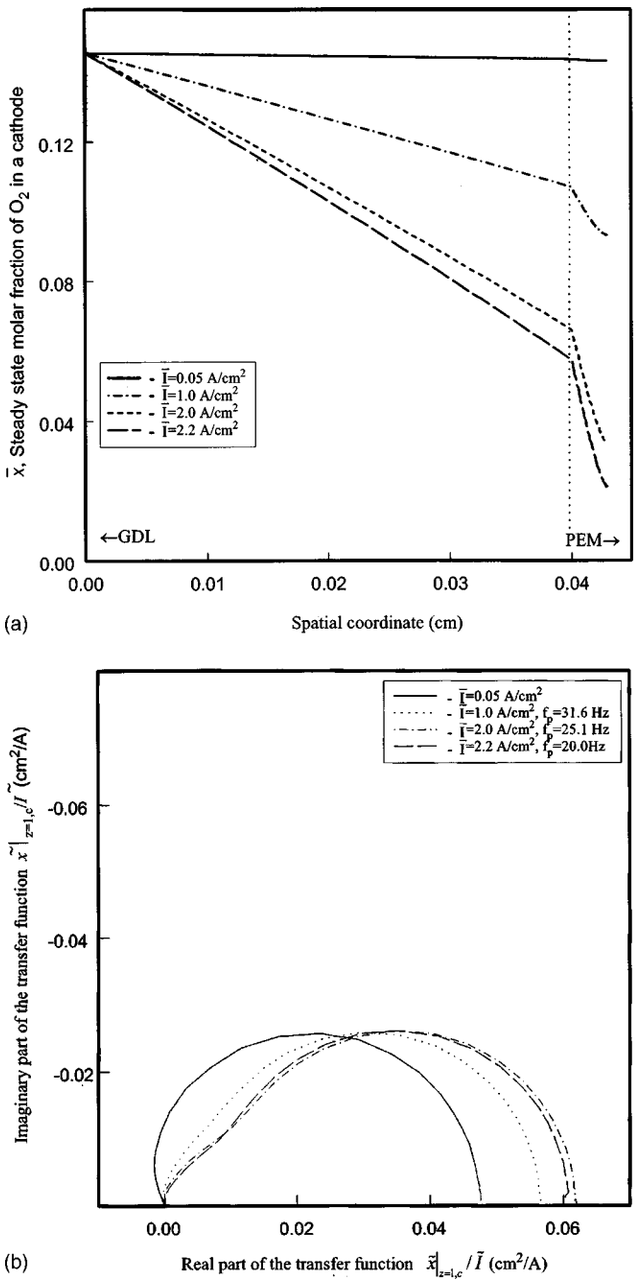

Figure 5. (a) Steady-state distribution of the mole fraction of O_2 in a PEMFC air cathode operated under the ambient gas pressure. (b) Transfer function for the deviation of the mole fraction of O_2, $\tilde{x}|_{z=1,c}/\tilde{I}$, on the PEM side of the CAL of a PEMFC air cathode operated under the ambient gas pressure.

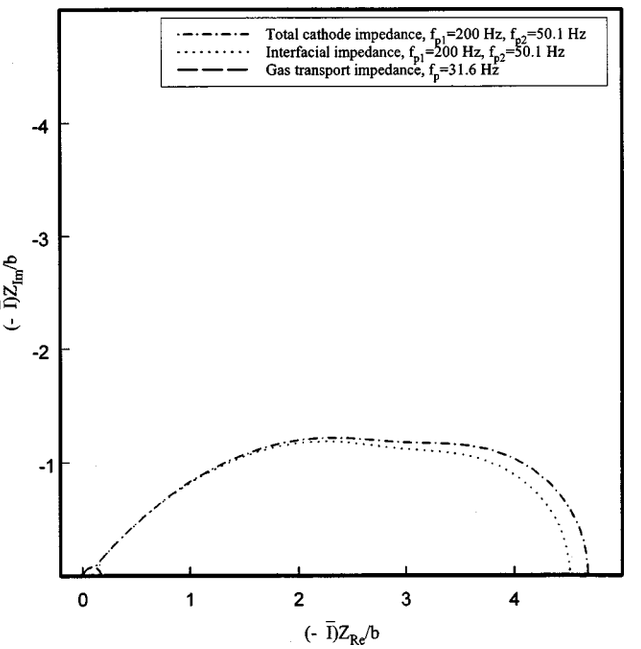

Figure 6. Comparison of the normalized impedance response of a full PEMFC air cathode operated under the ambient gas pressure with contributions from different sources. The steady-state operating current density $-\bar{I}$ is 1.0 A/cm^2.

$(4Fl_c\int_0^1\tilde{j}_O dz)/\tilde{I}$ involves an integration of $\tilde{j}_O$ over the entire CAL and is expected to reflect a shorter O_2 transport path in the gas phase.

To glean more information from the low-frequency impedance loops predicted at high steady-state operating current densities in Fig. 3, let us look at Fig. 5a, where the distributions of the steady-state mole fraction of O_2 in the gas pores of a PEMFC air cathode operated under the ambient gas pressure are presented, and Fig. 5b where the profiles for $\tilde{x}|_{c=1,c}/\tilde{I}$, the transfer function for the deviation of the mole fraction of O_2 on the PEM side of the CAL, are shown. Even if the steady-state mole fraction of O_2 adjacent to the PEM drops significantly with the increase of the steady-state operating current density (Fig. 5a), the transfer function $\tilde{x}|_{c=1,c}/\tilde{I}$ profile does not change much (Fig. 5b). As a result, the size of $\tilde{x}/\bar{x}|_{z=1,c}/\tilde{I}$ profile grows with the increase of the steady-state operating current density. This explains that for an air cathode, the low-frequency impedance loop increases its size with the increase of the steady-state operating current density (see Eq. 59).

We recall from Eq. 50 that the total impedance response of a PEMFC air cathode includes two contributions. One is from $\tilde{E}/\tilde{I}$, the impedance of gas-phase transport, and another is from $\tilde{\eta}/\tilde{I}$, an interfacial impedance. The computer simulation of the impedance response of a PEMFC cathode allows the separation of the total cathode impedance into the contributions from different sources, which is helpful for us in evaluating the relative importance of each impedance contribution. A comparison of the normalized impedance response of an air cathode, operated under the ambient gas pressure and at the steady-state operating current density equal to 1.0 A/cm^2, with the normalized impedance contributions from the gas-phase transport impedance and the interfacial impedance is shown in Fig. 6. As noticed, the cathode impedance is predominately contributed by the interfacial impedance, and the contribution from the gas-phase mass-transport impedance is small. Once more, let us consider a simple air cathode with an ultrathin CAL. There are two terms in Eq. 59, where the first one is the normalized impedance contribution from the interfacial impedance and the second term is the contribution from the gas-phase transport impedance. Because both terms involve $\tilde{x}/(\bar{x}\tilde{I})$, which is related to gas-phase transport limitation, we can conclude that the low-frequency impedance loop of an air cathode operated at a high steady-state current density reflects the combined effect of the gas-phase transport limitation and the effective charge-transfer resistance (see the first term of Eq. 59). If the effective charge-transfer resistance is overestimated, we can conclude from the first term of Eq. 59 that the low-frequency impedance loop will be underestimated. This explains the underestimation error

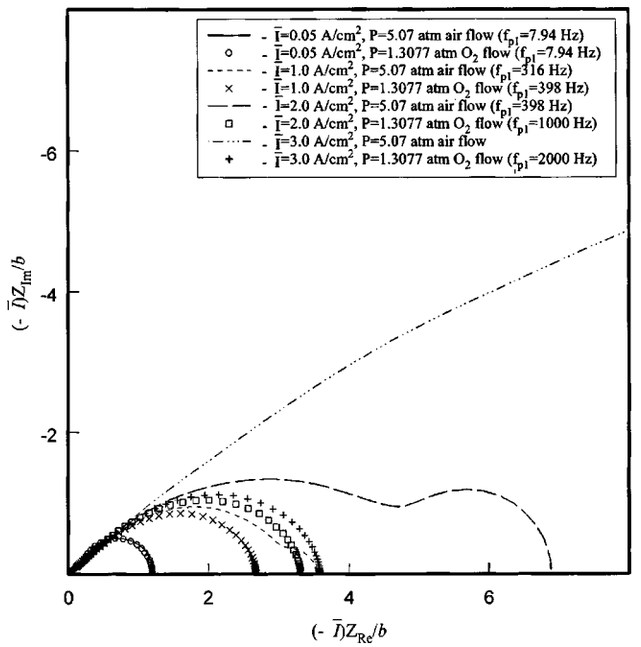

Figure 7. Comparison of the normalized impedance responses of an air cathode with those of an O_2 cathode. Both the air flow and O_2 flow have the same partial pressure of O_2.

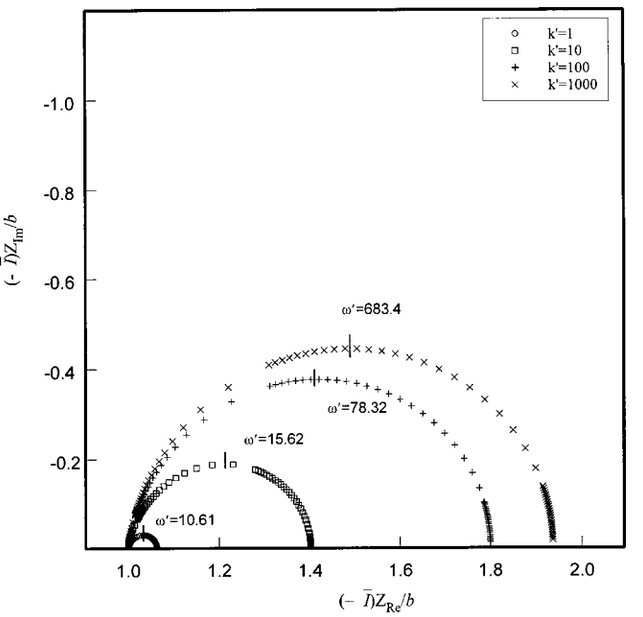

Figure 8. Comparison of the normalized impedance responses of an O_2 cathode with an ultrathin CAL under different steady-state operating conditions. Double-layer charging is not considered.

for the low-frequency impedance loops generated by the simplified model in Fig. 3.

To understand the difference between an air cathode and an O_2 cathode, it is helpful to look at Fig. 7, where the normalized impedance responses of a high pressure air cathode are compared with those of a low pressure O_2 cathode for different steady-state operating current densities. It is seen that at a very small operating current density, *i.e.*, $-\bar{I} = 0.05$ A/cm^2, both the air cathode and the O_2 cathode exhibit almost the same impedance profile and a normal Tafel slope. This indicates the absence of gas-phase transport limitation. With the increase of the steady-state operating current density, the O_2 cathode begins to display an increasingly apparent Tafel slope. When the steady-state operating current is equal to 3.0 A/cm^2, an almost quadric Tafel slope is obtained on the O_2 cathode, which is caused by a combined limitation from slow ionic conduction and slow dissolved O_2 diffusion.[4] For an air cathode, besides the increasing Tafel slope observed from the high-frequency impedance loop with the increase of the steady-state current density, a second impedance loop begins to grow and adds an extra Tafel slope. As explained above, this extra Tafel slope is the combined effect of the gas-phase transport limitation and the effective charge-transfer resistance. In Fig. 7, the peak frequency for the high-frequency impedance loop increases with the increase of the steady-state operating current density. An explanation is that the charge-transfer resistance decreases with the increase of the steady-state operating current density and consequently leads to the decrease of the time constant for the charge-transfer reaction and double-layer charging.

One might suspect that, in addition to the high-frequency impedance loop associated with the effective charge-transfer resistance and double-layer charging, the liquid-phase diffusion of O_2 inside an agglomerate particle is able to yield a low-frequency semicircle-like loop on the impedance plot of an O_2 cathode. To evaluate this possibility, let us consider a simple O_2 cathode with an ultrathin CAL. After neglecting double-layer charging, Eq. 34 is normalized to yield

$$(-\bar{I})\frac{Z}{b} = \frac{\sqrt{k'}\coth(\sqrt{k'}) - 1}{\sqrt{k' + j\omega'}\coth(\sqrt{k' + j\omega'}) - 1} \Bigg/ \frac{1 + j\frac{\omega'}{k'} - \left(1 - j\frac{\omega'}{k'}\right)[\sqrt{k'}\coth(\sqrt{k'}) - 1]}{j\frac{\omega'}{k'}} \qquad [62]$$

where

$$\omega' = \varepsilon\omega \Big/ \left(\frac{\varepsilon^{1+p}D}{R_a^{\,2}}\right) \qquad [63]$$

The impedance responses of the O_2 cathode under different steady-state operating conditions are compared in Fig. 8. One may notice that a semicircle-like impedance loop is indeed predicted even if double-layer charging is not considered. With the increase of k', the impedance loop grows to a semicircle with its diameter up to 2. However, if we look at the dimensionless peak frequency ω' for the impedance loop, we can find that ω' increases with the increase of k' (or the steady-state operating current density). This behavior indicates that it is very unlikely that the diffusion process inside an agglomerate particle yields a low-frequency impedance loop since its peak frequency has never been observed experimentally to become bigger and bigger with the increase of the steady-state operating current density.

An optimization of a PEMFC cathode is usually associated with overcoming one or more transport limitations, such as the mass-transport limitations in both the gas and liquid phase. In this work, the influences of the change of some important parameters, such as l_c/κ_{eff}, $i_{ref}/(4Fc_{ref})$, l_B, and R_a, on the electrode performance are briefly studied for an air cathode operated under the ambient gas pressure, and these results are presented in Fig. 9a-d. The polarization curves in Fig. 9a show that the decreases of l_c/κ_{eff}, l_B, and R_a as well as the increase of $i_{ref}/(4Fc_{ref})$ lead to the improvements of the cathode performance over a wide range of operating current

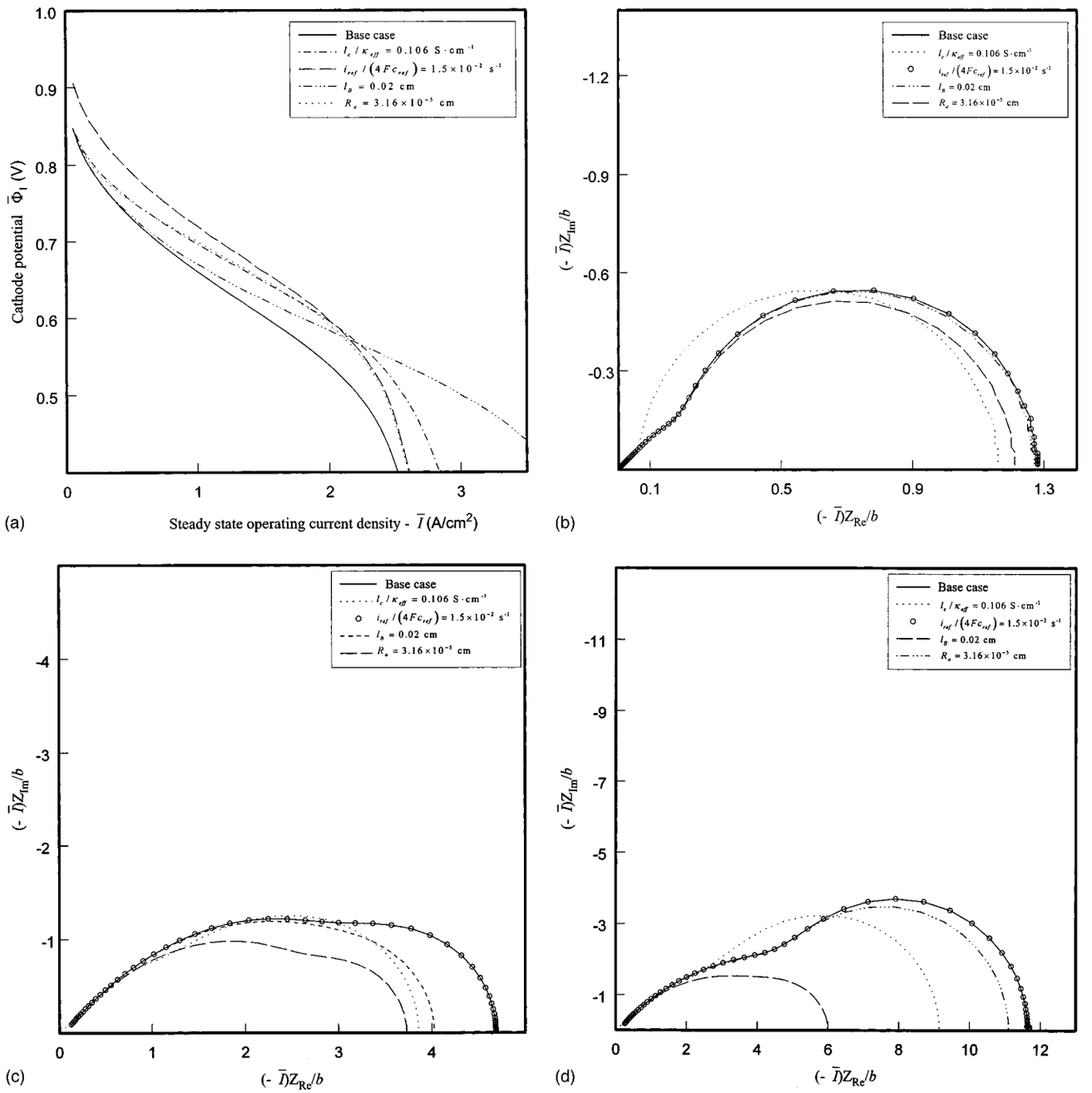

Figure 9. (a) Comparison of the polarization curves of a PEMFC air cathode operated under the ambient gas pressure. Only one parameter value is changed at one time. (b) Comparison of the normalized impedance responses of a PEMFC air cathode operated under the ambient gas pressure and at the steady-state operating current density $-\bar{I}$ = 0.05 A/cm^2. Only one parameter value is changed at one time. (c) Comparison of the normalized impedance responses of a PEMFC air cathode operated under the ambient gas pressure and at the steady-state operating current density $-\bar{I}$ = 1.0 A/cm^2. Only one parameter value is changed at one time. (d) Comparison of the normalized impedance responses of a PEMFC air cathode operated under the ambient gas pressure and at the steady state operating current density $-\bar{I}$ = 2.0 A/cm^2. Only one parameter value is changed at one time.

densities. Moreover, the decrease of l_B yields a much larger limiting current, which is expected to be caused by the decrease of the gas-phase transport path. The impedance responses calculated at the steady-state operating current densities equal to 0.05, 1.0, and 2.0 A/cm^2 are plotted in Fig. 9b-d. One may notice that the increase of $i_{ref}/(4Fc_{ref})$ does not cause any change of the steady-state impedance response. However, one should not simply conclude that $i_{ref}/(4Fc_{ref})$ has no influence on the cathode performance. The polarization curves in Fig. 9a demonstrate clearly the improvement of the cathode performance due to an increase of $i_{ref}/(4Fc_{ref})$. An explanation for the insensitivity of the steady-state impedance response to the change of $i_{ref}/(4Fc_{ref})$ is available in Appendix D. In Fig. 9b-d, we also observe that the decrease of any of the other parameters, l_c/κ_{eff}, $R_a l_B$, causes the decrease of the apparent Tafel slope, an indication of the improvement of existing mass-transport limitations.

Discussion.—The peak frequency for the second impedance loop

(low-frequency region) is an important characteristic quantity, from which the length of the mass-transport path in the gas pores can be possibly determined. If the mass-transport path in the gas phase were fixed, one would expect to observe an almost constant peak frequency, which can be verified by evaluating Eq. 11 of Ref. 6. However, special care must be taken before too much credit is given to this characteristic frequency. Figure 3 shows that this quantity decreases slightly with the increase of the steady-state operating current density. One explanation is the increase of the gas-phase transport path, and another explanation is the decrease of overlapping between the high-frequency impedance loop and the low-frequency loop.

In our previous impedance experiments on a PEMFC with an O_2 cathode, we sometimes observed two impedance loops at a steady-state operating current density larger than 2.0 A/cm^2, especially for a PEMFC with a poorly humidified H_2 anode. This low-frequency impedance loop exhibited almost the same peak frequency, *i.e.*, 20.0 Hz, even though its size usually grew with the increase of the steady-state current density. If this low-frequency impedance loop is generated from the O_2 cathode, the validity of the model developed in this work may be jeopardized because this model is able to predict only one impedance loop for an O_2 cathode. Because the liquid-phase diffusion of O_2 inside an agglomerate particle does not generate a low-frequency impedance loop, one might suspect that each agglomerate particle is covered by a very thin liquid film.[4] Also, the dissolved O_2 has to diffuse across this liquid barrier before reaching the catalyst sites. To exploit the possibility of attributing the low-frequency impedance loop of an O_2 cathode to the thin liquid film diffusion, Springer *et al.*'s impedance solution for a planar liquid film diffusion model is useful[7]

$$Z = \frac{b\left(1 + i^* \exp\left(-\frac{\overline{\eta}}{b}\right) \Big/ I_F\right)}{i^* \exp\left(-\frac{\overline{\eta}}{b}\right)} + \frac{b\left(1 + i^* \exp\left(-\frac{\overline{\eta}}{b}\right) \Big/ I_F\right)}{I_F} \frac{\tanh(\sqrt{j\omega l^2/D})}{\sqrt{j\omega l^2/D}} \quad [64]$$

where i^* is the effective exchange current density for the O_2 reduction reaction, l is the thickness of the liquid film, and I_F is a characteristic current density. After evaluating Eq. 64, we can find the impedance peak frequency f_p from

$$\frac{2\pi f_p l^2}{D} = 2.5406 \quad [65]$$

By using a value of 20.0 Hz for the experimentally observed impedance peak frequency and a value of 6.22×10^{-6} cm^2/s for D, we can find from Eq. 65 that $l = 3.55$ μm. To have such a thick liquid film outside each agglomerate particle, an average pore size (diameter) of no less than 7.1 μm in the CAL is required. This is unlikely to be true. Therefore, we conclude that the attribution of a low frequency impedance loop observed on an O_2/H_2 PEMFC to the O_2 cathode is not justified by the thin liquid film diffusion. The poor water management in the PEM may be useful for explaining this low frequency impedance loop.[13] Unfortunately, the study of the water management in the PEM is not covered in the present work.

Conclusions

A steady-state impedance model for a PEMFC cathode is presented in this work to include the feature of multicomponent gas transport in the CAL. Two impedance loops are predicted for an air cathode at high steady-state operating current densities. The high-frequency impedance loop is attributed to the effective charge-transfer resistance and double-layer charging, and the low-frequency loop is attributed to a combined effect of the gas-phase transport limitation and the effective charge-transfer resistance.

Acknowledgments

The authors are grateful for the financial support of this project by Hybrid Advanced Power Sources by the National Reconnaissance Office (NRO) under contract no. NRO-000-01-C-4368.

University of South Carolina assisted in meeting the publication costs of this article.

Appendix A

Under a steady-state operating condition, Eq. 21 is simplified to

$$\frac{\varepsilon^{1+p_D} D}{R_a^2} \frac{1}{r^2} \frac{\partial}{\partial r}\left(r^2 \frac{\partial \overline{c}}{\partial r}\right) - \overline{k}\overline{c} = 0 \quad [A\text{-}1]$$

subject to boundary conditions

$$\left.\frac{\partial \overline{c}}{\partial r}\right|_{r=0} = 0 \quad [A\text{-}2]$$

$$\overline{c}|_{r=1} = c_G H \overline{x} \quad [A\text{-}3]$$

After substituting $\overline{c} = \overline{C}/r$ into Eq. A-1, we have

$$\frac{\partial^2 \overline{C}}{\partial r^2} - \frac{\overline{k}}{\frac{\varepsilon^{1+p_D} D}{R_a^2}} \overline{C} = 0 \quad [A\text{-}4]$$

from which we can write the solution of $\overline{C}$ as

$$\overline{C} = r\overline{c} = c_1 \sinh\left(\sqrt{\frac{\overline{k}}{\frac{\varepsilon^{1+p_D} D}{R_a^2}}}\, r\right) + c_2 \cosh\left(\sqrt{\frac{\overline{k}}{\frac{\varepsilon^{1+p_D} D}{R_a^2}}}\, r\right) \quad [A\text{-}5]$$

where c_1 and c_2 are constants.

After applying boundary conditions A-2 and A-3 to Eq. A-5, we can find

$$c_1 = \frac{c_G H \overline{x}}{\sinh\left(\sqrt{\frac{\overline{k}}{\frac{\varepsilon^{1+p_D} D}{R_a^2}}}\right)}, \quad c_2 = 0 \quad [A\text{-}6]$$

Equation A-5 is updated with Eq. A-6 to yield

$$\overline{c} = c_G H \overline{x} \frac{\sinh\left(\sqrt{\frac{\overline{k}}{\frac{\varepsilon^{1+p_D} D}{R_a^2}}}\, r\right)}{r \sinh\left(\sqrt{\frac{\overline{k}}{\frac{\varepsilon^{1+p_D} D}{R_a^2}}}\right)} \quad [A\text{-}7]$$

The steady-state reaction current per unit volume of the CAL, $4F\overline{j_e}$, can be calculated by either

$$4F\overline{j_e} = -12F(1-\varphi_c)\int_0^1 \overline{k}\overline{c}r^2 dr$$

$$= -12F(1-\varphi_c)\frac{\varepsilon^{1+p}D}{R_a^2}c_G H\overline{x}\left[\sqrt{\frac{\overline{k}}{\frac{\varepsilon^{1+p}D}{R_a^2}}}\coth\left(\sqrt{\frac{\overline{k}}{\frac{\varepsilon^{1+p}D}{R_a^2}}}\right) - 1\right] \quad [A\text{-}8]$$

or

$$4F\overline{j_O} = -12F(1-\varphi_c)\frac{\varepsilon^{1+p}D}{R_a^2}\left.\frac{\partial\overline{c}}{\partial z}\right|_{z=1}$$

$$= -12F(1-\varphi_c)\frac{\varepsilon^{1+p}D}{R_a^2}c_G H\overline{x}$$

$$\times\left[\sqrt{\frac{\overline{k}}{\frac{\varepsilon^{1+p}D}{R_a^2}}}\coth\left(\sqrt{\frac{\overline{k}}{\frac{\varepsilon^{1+p}D}{R_a^2}}}\right) - 1\right] \quad [A\text{-}9]$$

For a dynamic model, substitution of $\tilde{c} = \tilde{C}/r$ and Eq. A-7 into Eq. 29 yields

$$\frac{\partial^2\tilde{C}}{\partial r^2} - \frac{\overline{k}+j\varepsilon\omega}{\frac{\varepsilon^{1+p}D}{R_a^2}}\tilde{C} + \frac{\overline{k}}{\frac{\varepsilon^{1+p}D}{R_a^2}}c_G H\overline{x}\frac{\tilde{\eta}}{b}\frac{\sinh\left(\sqrt{\frac{\overline{k}}{\frac{\varepsilon^{1+p}D}{R_a^2}}}r\right)}{\sinh\left(\sqrt{\frac{\overline{k}}{\frac{\varepsilon^{1+p}D}{R_a^2}}}\right)} = 0 \quad [A\text{-}10]$$

from which we can write the solution of $\tilde{C}$ as

$$\tilde{C} = r\tilde{c} = c_3\sinh\left(\sqrt{\frac{\overline{k}+j\varepsilon\omega}{\frac{\varepsilon^{1+p}D}{R_a^2}}}r\right) + c_4\cosh\left(\sqrt{\frac{\overline{k}+j\varepsilon\omega}{\frac{\varepsilon^{1+p}D}{R_a^2}}}r\right) + \frac{\tilde{\eta}}{b}\frac{\sinh\left(\sqrt{\frac{\overline{k}}{\frac{\varepsilon^{1+p}D}{R_a^2}}}r\right)}{j\frac{\varepsilon\omega}{\overline{k}}\sinh\left(\sqrt{\frac{\overline{k}}{\frac{\varepsilon^{1+p}D}{R_a^2}}}\right)}c_G H\overline{x} \quad [A\text{-}11]$$

where c_3 and c_4 are constants. After applying boundary condition Eq. 30 and 31, we can determine

$$c_3 = c_G H\overline{x}\left[\frac{\frac{\tilde{x}}{\overline{x}}}{\sinh\left(\sqrt{\frac{\overline{k}+j\varepsilon\omega}{\frac{\varepsilon^{1+p}D}{R_a^2}}}\right)} - \frac{\frac{\tilde{\eta}}{b}}{j\frac{\varepsilon\omega}{k}\sinh\left(\sqrt{\frac{\overline{k}+j\varepsilon\omega}{\frac{\varepsilon^{1+p}D}{R_a^2}}}\right)}\right], \quad c_4 = 0 \quad [A\text{-}12]$$

Equation A-11 is updated with Eq. A-12 to yield

$$\tilde{c} = c_G H\overline{x}\left\{\frac{\sinh\left(\sqrt{\frac{\overline{k}+j\varepsilon\omega}{\frac{\varepsilon^{1+p}D}{R_a^2}}}r\right)}{r\sinh\left(\sqrt{\frac{\overline{k}+j\varepsilon\omega}{\frac{\varepsilon^{1+p}D}{R_a^2}}}\right)}\frac{\tilde{x}}{\overline{x}} - \frac{\tilde{\eta}}{b}\frac{\frac{\sinh\left(\sqrt{\frac{\overline{k}+j\varepsilon\omega}{\frac{\varepsilon^{1+p}D}{R_a^2}}}r\right)}{r\sinh\left(\sqrt{\frac{\overline{k}+j\varepsilon\omega}{\frac{\varepsilon^{1+p}D}{R_a^2}}}\right)} - \frac{\sinh\left(\sqrt{\frac{\overline{k}}{\frac{\varepsilon^{1+p}D}{R_a^2}}}r\right)}{r\sinh\left(\sqrt{\frac{\overline{k}}{\frac{\varepsilon^{1+p}D}{R_a^2}}}\right)}}{j\frac{\varepsilon\omega}{\overline{k}}}\right\} \quad [A\text{-}13]$$

The deviation of the accumulation rate of O_2, $\tilde{j}_O$, in the gas phase per unit volume of the CAL can be calculated by substituting Eq. A-13 into Eq. 26

$$\tilde{j}_O = -3(1-\varphi_c)\frac{\varepsilon^{1+p}D}{R_a^2}c_G H\overline{x}\times\left\{\left[\sqrt{\frac{(\overline{k}+j\varepsilon\omega)}{\frac{\varepsilon^{1+p}D}{R_a^2}}}\coth\left(\sqrt{\frac{(\overline{k}+j\varepsilon\omega)}{\frac{\varepsilon^{1+p}D}{R_a^2}}}\right) - 1\right]\frac{\tilde{x}}{\overline{x}}\right.$$

$$\left. - \frac{-\tilde{\eta}}{b}\frac{\sqrt{\frac{(\overline{k}+j\varepsilon\omega)}{\frac{\varepsilon^{1+p}D}{R_a^2}}}\coth\left(\sqrt{\frac{(\overline{k}+j\varepsilon\omega)}{\frac{\varepsilon^{1+p}D}{R_a^2}}}\right) - \sqrt{\frac{\overline{k}}{\frac{\varepsilon^{1+p}}{R_a^2}}}\coth\left(\sqrt{\frac{\overline{k}}{\frac{\varepsilon^{1+p}D}{R_a^2}}}\right)}{j\frac{\varepsilon\omega}{\overline{k}}}\right\} \quad [A\text{-}14]$$

The deviation of the O_2 reduction current per unit volume of the CAL can be calculated by substituting Eq. A-13 into Eq. 25

$$4F\tilde{j}_e = -12F(1-\varphi_c)\frac{\varepsilon^{1+p}D}{R_a^2}c_G H\bar{x}\times\left\{\begin{array}{l}\dfrac{\sqrt{\dfrac{(\bar{k}+j\varepsilon\omega)}{\dfrac{\varepsilon^{1+p}D}{R_a^2}}}\coth\left(\sqrt{\dfrac{(\bar{k}+j\varepsilon\omega)}{\dfrac{\varepsilon^{1+p}D}{R_a^2}}}\right)-1}{1+j\dfrac{\varepsilon\omega}{\bar{k}}}\dfrac{\tilde{x}}{\bar{x}} \\ \dfrac{\sqrt{\dfrac{(\bar{k}+j\varepsilon\omega)}{\dfrac{\varepsilon^{1+p}D}{R_a^2}}}\coth\left(\sqrt{\dfrac{(\bar{k}+j\varepsilon\omega)}{\dfrac{\varepsilon^{1+p}D}{R_a^2}}}\right)-1}{1+j\dfrac{\varepsilon\omega}{\bar{k}}}-\left(1-j\dfrac{\varepsilon\omega}{\bar{k}}\right)\left[\sqrt{\dfrac{\bar{k}}{\dfrac{\varepsilon^{1+p}D}{R_a^2}}}\coth\left(\sqrt{\dfrac{\bar{k}}{\dfrac{\varepsilon^{1+p}D}{R_a^2}}}\right)-1\right] \\ \dfrac{\tilde{\eta}}{b}\dfrac{}{j\dfrac{\varepsilon\omega}{\bar{k}}}\end{array}\right\} \quad [A\text{-}15]$$

Appendix B

For an O_2 cathode, the steady-state overpotential profile in the CAL is found by solving

$$\frac{\partial^2\bar{\eta}}{\partial z^2} = \frac{l_c}{\kappa_{eff}}4F\bar{j}_e l_c \quad [B\text{-}1]$$

subject to boundary conditions

$$\left.\frac{\partial\bar{\eta}}{\partial z}\right|_{z=0,c} = 0 \quad [B\text{-}2]$$

and

$$\left.\frac{\partial\bar{\eta}}{\partial z}\right|_{z=1,c} = \frac{l_c}{\kappa_{eff}}\bar{I} \quad [B\text{-}3]$$

The deviation profiles of $\tilde{\eta}_{Re}$ and $\tilde{\eta}_{Im}$ are found by solving

$$\frac{\partial^2\tilde{\eta}_{Re}}{\partial z^2} = \frac{l_c}{\kappa_{eff}}[4F\bar{j}_{e,Re}l_c - \omega(1-\varphi_c)(1-\varepsilon)C_{dl}l_c\tilde{\eta}_{Im}] \quad [B\text{-}4]$$

and

$$\frac{\partial^2\tilde{\eta}_{Im}}{\partial z^2} = \frac{l_c}{\kappa_{eff}}[4F\tilde{j}_{e,Im}l_c + \omega(1-\varphi_c)(1-\varepsilon)C_{dl}l_c\tilde{\eta}_{Re}] \quad [B\text{-}5]$$

subject to boundary conditions

$$\left.\frac{\partial\tilde{\eta}_{Re}}{\partial z}\right|_{z=0,c} = 0, \quad \left.\frac{\partial\tilde{\eta}_{Im}}{\partial z}\right|_{z=0,c} = 0 \quad [B\text{-}6]$$

and

$$\left.\frac{\partial\tilde{\eta}_{Re}}{\partial z}\right|_{z=1,c} = \frac{l_c}{\kappa_{eff}}, \quad \left.\frac{\partial\tilde{\eta}_{Im}}{\partial z}\right|_{z=1,c} = 0 \quad [B\text{-}7]$$

The steady-state impedance responses, Z_{Re} and Z_{Im}, of an O_2 cathode can be calculated by

$$Z_{Re} = \tilde{\eta}_{Re}|_{z=1,c} \quad \text{and} \quad Z_{Im} = \tilde{\eta}_{Im}|_{z=1,c} \quad [B\text{-}8]$$

For an air cathode, the steady-state mole fraction of O_2 profile in the GDL is found by solving

$$\frac{\beta_1+\beta_2\bar{x}}{(\beta_1-\bar{x})(\beta_3+\beta_2\bar{x})}\frac{\partial\bar{x}}{\partial z} = \frac{\bar{I}}{4F\varphi_B{}^{1+p}D^0_{ON}c_G/l_B} \quad [B\text{-}9]$$

subject to boundary condition

$$\bar{x}|_{z=0,b} = x_0 \quad [B\text{-}10]$$

where x_0 is the mole fraction of O_2 at the inlet of the GDL.

The steady-state mole fraction of O_2 profile in the CAL is found by solving

$$\frac{\beta_1+\beta_2\bar{x}}{(\beta_1-\bar{x})(\beta_3+\beta_2\bar{x})}\frac{\partial^2\bar{x}}{\partial z^2} + \frac{\beta_4+2\beta_1\beta_2\bar{x}+\beta_2{}^2\bar{x}^2}{(\beta_1-\bar{x})^2(\beta_3+\beta_2\bar{x})^2}\left(\frac{\partial\bar{x}}{\partial z}\right)^2 = \frac{-\bar{j}_0 l_c}{\varphi_c{}^{1+p}D^0_{ON}c_G/l_c} \quad [B\text{-}11]$$

subject to boundary conditions

$$\bar{x}|_{z=0,c} = \bar{x}|_{z=1,B} \quad [B\text{-}12]$$

and

$$\left.\frac{\partial\bar{x}}{\partial z}\right|_{z=1,c} = 0 \quad [B\text{-}13]$$

The steady-state overpotential profile in the CAL is found by solving

$$\frac{\partial^2\bar{\eta}}{\partial z^2} = \frac{l_c}{\kappa_{eff}}4F\bar{j}_e l_c - \frac{RT}{4F}\frac{\partial^2\ln\bar{x}}{\partial z^2} \quad [B\text{-}14]$$

subject to boundary conditions

$$\left.\frac{\partial\bar{\eta}}{\partial z}\right|_{z=0,c} = -\frac{RT}{4F}\left.\frac{\partial\ln(\bar{x})}{\partial z}\right|_{z=0,c} \quad [B\text{-}15]$$

and

$$\left.\frac{\partial\bar{\eta}}{\partial z}\right|_{z=0,c} = \frac{l_c}{\kappa_{eff}}\bar{I} \quad [B\text{-}16]$$

The deviation profiles of $\tilde{x}_{Re}$, $\tilde{x}_{Im}$, $\tilde{\eta}_{Re}$, and $\tilde{\eta}_{Im}$ are found by solving

$$\frac{\beta_1+\beta_2\bar{x}}{\beta_3+\beta_2\bar{x}}\frac{\partial^2\tilde{x}_{Re}}{\partial z^2} + \left[2\frac{\beta_2(\beta_3-\beta_1)}{(\beta_3+\beta_2\bar{x})^2}\frac{\partial\bar{x}}{\partial z} + \frac{\bar{I}/4F}{\varphi_B{}^{1+p}D^0_{ON}c_G/l_B}\right]\frac{\partial\tilde{x}_{Re}}{\partial z} + \left[\frac{\beta_2(\beta_3-\beta_1)}{(\beta_3+\beta_2\bar{x})^2}\frac{\partial^2\bar{x}}{\partial z^2} - 2\left(\frac{\partial\bar{x}}{\partial z}\right)^2\frac{(\beta_3-\beta_1)\beta_2{}^2}{(\beta_3+\beta_2\bar{x})^3}\right]\tilde{x}_{Re} + \frac{\beta_1\varphi_B\omega}{\varphi_B{}^{1+p}D^0_{ON}/l_B{}^2}\tilde{x}_{Im} = -\frac{\partial\bar{x}}{\partial z}\frac{l_c\int_0^1\tilde{j}_{O,Re}dz}{\varphi_B{}^{1+p}D^0_{ON}c_G/l_B} \quad [B\text{-}17]$$

and

$$\frac{\beta_1+\beta_2\bar{x}}{\beta_3+\beta_2\bar{x}}\frac{\partial^2\tilde{x}_{Im}}{\partial z^2} + \left[2\frac{\beta_2(\beta_3-\beta_1)}{(\beta_3+\beta_2\bar{x})^2}\frac{\partial\bar{x}}{\partial z} + \frac{\bar{I}/4F}{\varphi_B{}^{1+p}D^0_{ON}c_G/l_B}\right]\frac{\partial\tilde{x}_{Im}}{\partial z} + \left[\frac{\beta_2(\beta_3-\beta_1)}{(\beta_3+\beta_2\bar{x})^2}\frac{\partial^2\bar{x}}{\partial z^2} - 2\left(\frac{\partial\bar{x}}{\partial z}\right)^2\frac{(\beta_3-\beta_1)\beta_2{}^2}{(\beta_3+\beta_2\bar{x})^3}\right]\tilde{x}_{Im} - \frac{\beta_1\varphi_B\omega}{\varphi_B{}^{1+p}D^0_{ON}/l_B{}^2}\tilde{x}_{Re} = -\frac{\partial\bar{x}}{\partial z}\frac{l_c\int_0^1\tilde{j}_{O,Im}dz}{\varphi_B{}^{1+p}D^0_{ON}c_G/l_B} \quad [B\text{-}18]$$

for the GDL and by solving

$$\frac{\beta_1+\beta_2\overline{x}}{\beta_3+\beta_2\overline{x}}\frac{\partial^2\widetilde{x}_{Re}}{\partial z^2}+\left[2\frac{\beta_2(\beta_3-\beta_1)}{(\beta_3+\beta_2\overline{x})^2}\frac{\partial\overline{x}}{\partial z}-\frac{-\overline{I}/4F+l_c\int_0^z\overline{j}_O dz}{\varphi_c{}^{1+p}D_{ON}^0c_G/l_c}\right]\frac{\partial\widetilde{x}_{Re}}{\partial z}$$
$$+\left[-\frac{l_c\overline{j}_O}{\varphi_c{}^{1+p}D_{ON}^0c_G/l_c}+\frac{\beta_2(\beta_3-\beta_1)}{(\beta_3+\beta_2\overline{x})^2}\frac{\partial^2\overline{x}}{\partial z^2}-2\left(\frac{\partial\overline{x}}{\partial z}\right)^2\frac{(\beta_3-\beta_1)\beta_2{}^2}{(\beta_3+\beta_2\overline{x})^3}\right]\widetilde{x}_{Re}$$
$$+\frac{\beta_1\varphi_c\omega}{\varphi_c{}^{1+p}D_{ON}^0/l_c{}^2}\widetilde{x}_{Im}+\frac{\beta_1-\overline{x}}{\varphi_c{}^{1+p}D_{ON}^0c_G/l_c}l_c\widetilde{j}_{O,Re}$$
$$=\frac{\partial\overline{x}}{\partial z}\frac{-l_c\int_0^1\widetilde{j}_{O,Re}dz+l_c\int_0^z\widetilde{j}_{O,Re}dz}{\varphi_c{}^{1+p}D_{ON}^0c_G/l_c} \qquad [B\text{-}19]$$

$$\frac{\beta_1+\beta_2\overline{x}}{\beta_3+\beta_2\overline{x}}\frac{\partial^2\widetilde{x}_{Im}}{\partial z^2}+\left[2\frac{\beta_2(\beta_3-\beta_1)}{(\beta_3+\beta_2\overline{x})^2}\frac{\partial\overline{x}}{\partial z}-\frac{-\overline{I}/4F+l_c\int_0^z\overline{j}_O dz}{\varphi_c{}^{1+p}D_{ON}^0c_G/l_c}\right]\frac{\partial\widetilde{x}_{Im}}{\partial z}$$
$$+\left[-\frac{l_c\overline{j}_O}{\varphi_c{}^{1+p}D_{ON}^0c_G/l_c}+\frac{\beta_2(\beta_3-\beta_1)}{(\beta_3+\beta_2\overline{x})^2}\frac{\partial^2\overline{x}}{\partial z^2}-2\left(\frac{\partial\overline{x}}{\partial z}\right)^2\frac{(\beta_3-\beta_1)\beta_2{}^2}{(\beta_3+\beta_2\overline{x})^3}\right]\widetilde{x}_{Im}$$
$$-\frac{\beta_1\varphi_c\omega}{\varphi_c{}^{1+p}D_{ON}^0/l_c{}^2}\widetilde{x}_{Re}+\frac{\beta_1-\overline{x}}{\varphi_c{}^{1+p}D_{ON}^0c_G/l_c}l_c\widetilde{j}_{O,Im}$$
$$=\frac{\partial\overline{x}}{\partial z}\frac{-l_c\int_0^1\widetilde{j}_{O,Im}dz+l_c\int_0^z\widetilde{j}_{O,Im}dz}{\varphi_c{}^{1+p}D_{ON}^0c_G/l_c} \qquad [B\text{-}20]$$

$$\frac{\partial^2\widetilde{\eta}_{Re}}{\partial z^2}=\frac{l_c}{\kappa_{eff}}[4F\widetilde{j}_{e,Re}l_c-\omega(1-\varphi_c)(1-\varepsilon)C_{dl}l_c\widetilde{\eta}_{Im}]-\frac{RT}{4F}\frac{\partial^2\left(\frac{\widetilde{x}_{Re}}{\overline{x}}\right)}{\partial z^2} \qquad [B\text{-}21]$$

and

$$\frac{\partial^2\widetilde{\eta}_{Im}}{\partial z^2}=\frac{l_c}{\kappa_{eff}}[4F\widetilde{j}_{e,Im}l_c+\omega(1-\varphi_c)(1-\varepsilon)C_{dl}l_c\widetilde{\eta}_{Re}]-\frac{RT}{4F}\frac{\partial^2\left(\frac{\widetilde{x}_{Im}}{\overline{x}}\right)}{\partial z^2} \qquad [B\text{-}22]$$

for the CAL. Equations B-17 through B-22 are subject to the following boundary conditions

$$\widetilde{x}_{Re}|_{z=0,B}=0,\ \widetilde{x}_{Im}|_{z=0,B}=0 \qquad [B\text{-}23]$$

$$\frac{\varphi_B{}^{1+p}}{l_B}\frac{\partial\widetilde{x}_{Re}}{\partial z}\bigg|_{z=1,B}=\frac{\varphi_c{}^{1+p}}{l_c}\frac{\partial\widetilde{x}_{Re}}{\partial z}\bigg|_{z=0,c},\ \frac{\varphi_B{}^{1+p}}{l_B}\frac{\partial\widetilde{x}_{Im}}{\partial z}\bigg|_{z=1,B}=\frac{\varphi_c{}^{1+p}}{l_c}\frac{\partial\widetilde{x}_{Im}}{\partial z}\bigg|_{z=0,c} \qquad [B\text{-}24]$$

$$\frac{\partial\widetilde{x}_{Re}}{\partial z}\bigg|_{z=1,c}=0,\ \frac{\partial\widetilde{x}_{Im}}{\partial z}\bigg|_{z=1,c}=0 \qquad [B\text{-}25]$$

$$\frac{\partial\widetilde{\eta}_{Re}}{\partial z}\bigg|_{z=0,c}=-\frac{RT}{4F}\frac{\partial\left(\frac{\widetilde{x}_{Re}}{\overline{x}}\right)}{\partial z}\bigg|_{z=0,c},\ \frac{\partial\widetilde{\eta}_{Im}}{\partial z}\bigg|_{z=0,c}=-\frac{RT}{4F}\frac{\partial\left(\frac{\widetilde{x}_{Im}}{\overline{x}}\right)}{\partial z}\bigg|_{z=0,c} \qquad [B\text{-}26]$$

and

$$\frac{\partial\widetilde{\eta}_{Re}}{\partial z}\bigg|_{z=1,c}=\frac{l_c}{\kappa_{eff}},\ \frac{\partial\widetilde{\eta}_{Im}}{\partial z}\bigg|_{z=1,c}=0 \qquad [B\text{-}27]$$

The steady-state impedance responses, Z_{Re} and Z_{Im}, of an air cathode can be calculated by

$$Z_{Re}=\left(\frac{RT}{4F}\frac{\widetilde{x}_{Re}}{\overline{x}}+\widetilde{\eta}_{Re}\right)\bigg|_{z=1,c}\ \text{and}\ Z_{Im}=\left(\frac{RT}{4F}\frac{\widetilde{x}_{Im}}{\overline{x}}+\widetilde{\eta}_{Im}\right)\bigg|_{z=1,c} \qquad [B\text{-}28]$$

Appendix C

After splitting $\widetilde{j}_O$ into a real part, $\widetilde{j}_{O,Re}$, and an imaginary part, $j(\widetilde{j}_{O,Im})$, Eq. A-14 is expressed as

$$\widetilde{j}_O=\widetilde{j}_{O,Re}+j(\widetilde{j}_{O,Im})$$

where

$$\widetilde{j}_{O,Re}=-3(1-\varphi_c)\frac{\varepsilon^{1+p}D}{R_a{}^2}c_GH\overline{x}S_{31}$$

$$\widetilde{j}_{O,Im}=-3(1-\varphi_c)\frac{\varepsilon^{1+p}D}{R_a{}^2}c_GH\overline{x}S_{32}$$

where

$$S_{31}=(S_{21}-1)\frac{\widetilde{x}_{Re}}{\overline{x}}-S_{22}\frac{\widetilde{x}_{Im}}{\overline{x}}-\left\{[S_{21}-\sqrt{k'}\coth(\sqrt{k'})]\frac{\widetilde{\eta}_{Im}}{b}+S_{22}\frac{\widetilde{\eta}_{Re}}{b}\right\}\frac{k'}{\omega'}$$

$$S_{32}=(S_{21}-1)\frac{\widetilde{x}_{Im}}{\overline{x}}+S_{22}\frac{\widetilde{x}_{Re}}{\overline{x}}+\left\{[S_{21}-\sqrt{k'}\coth(\sqrt{k'})]\frac{\widetilde{\eta}_{Re}}{b}-S_{22}\frac{\widetilde{\eta}_{Im}}{b}\right\}\frac{k'}{\omega'}$$

where

$$S_{21}=\frac{S_{11}\sinh(S_{11})\cosh(S_{11})}{\sinh(S_{11})^2+\sin(S_{12})^2}+\frac{S_{12}\sin(S_{12})\cos(S_{12})}{\sinh(S_{11})^2+\sin(S_{12})^2}$$

$$S_{22}=\frac{S_{12}\sinh(S_{11})\cosh(S_{11})}{\sinh(S_{11})^2+\sin(S_{12})^2}-\frac{S_{11}\sin(S_{12})\cos(S_{12})}{\sinh(S_{11})^2+\sin(S_{12})^2}$$

where

$$S_{11}=\sqrt{\frac{\sqrt{k'^2+\omega'^2}+k'}{2}},\ S_{12}=\sqrt{\frac{\sqrt{k^{IH2}+\omega'^2}-k'}{2}} \qquad [C\text{-}1]$$

and where

$$k'=\frac{\overline{k}}{\frac{\varepsilon^{1+p}D}{R_a{}^2}},\ \omega'=\frac{\varepsilon\omega}{\frac{\varepsilon^{1+p}D}{R_a{}^2}}$$

After splitting $4F\widetilde{j}_e$ into a real part, $4F\widetilde{j}_{e,Re}$, and an imaginary part, $j(4F\widetilde{j}_{e,Im})$, Eq. A-15 is expressed as

$$4F\widetilde{j}_e=4F\overline{j}_{e,Re}+j(4F\widetilde{j}_{e,Im})$$

where

$$4F\overline{j}_{e,Re}=-12F(1-\varphi_c)\frac{\varepsilon^{1+p}D}{R_a{}^2}c_GH\overline{x}S_{41}$$

$$4F\widetilde{j}_{e,Im}=-12F(1-\varphi_c)\frac{\varepsilon^{1+p}D}{R_a{}^2}c_GH\overline{x}S_{42}$$

where

$$S_{41}=\frac{k'(S_{21}-1)+\omega'S_{22}}{k'\left(1+\frac{\omega'^2}{k'^2}\right)}\frac{\widetilde{x}_{Re}}{\overline{x}}-\frac{k'S_{22}-\omega'(S_{21}-1)}{k'\left(1+\frac{\omega'^2}{k'^2}\right)}\frac{\widetilde{x}_{Im}}{\overline{x}}$$
$$-\frac{\frac{k'S_{22}-\omega'(S_{21}-1)}{1+\frac{\omega'^2}{k'^2}}+\omega'[\sqrt{k'}\coth(\sqrt{k'})-1]}{\omega'}\frac{\widetilde{\eta}_{Re}}{b}$$
$$-\frac{\frac{k'(S_{21}-1)+\omega'S_{22}}{1+\frac{\omega'^2}{k'^2}}-k'[\sqrt{k'}\coth(\sqrt{k'})-1]}{\omega'}\frac{\widetilde{\eta}_{Im}}{b}$$

$$S_{42}=\frac{k'S_{22}-\omega'(S_{21}-1)}{k'\left(1+\frac{\omega'^2}{k'^2}\right)}\frac{\widetilde{x}_{Re}}{\overline{x}}+\frac{k'(S_{21}-1)+\omega'S_{22}}{k'\left(1+\frac{\omega'^2}{k'^2}\right)}\frac{\widetilde{x}_{Im}}{\overline{x}}$$
$$+\frac{\frac{k'(S_{21}-1)+\omega'S_{22}}{1+\frac{\omega'^2}{k'^2}}-k'[\sqrt{k'}\coth(\sqrt{k'})-1]}{\omega'}\frac{\widetilde{\eta}_{Re}}{b}$$
$$-\frac{\frac{k'S_{22}-\omega'(S_{21}-1)}{1+\frac{\omega'^2}{k'^2}}+\omega'[\sqrt{k'}\coth(\sqrt{k'})-1]}{\omega'}\frac{\widetilde{\eta}_{Im}}{b} \qquad [C\text{-}2]$$

where the expressions for S_{11}, S_{12}, S_{21}, S_{22}, k', and ω' are the same as those used in Eq. C-1.

Appendix D

Equation 28 can be rewritten as

$$\overline{\eta} = -b \ln \overline{k} + b \ln\left[\frac{i_{\text{ref}}}{4Fc_{\text{ref}}}(1-\varepsilon)\right] \quad \text{[D-1]}$$

Substitution of Eq. D-1 into Eq. B-14, B-15, and B-16 yields

$$-b\frac{\partial^2 \ln \overline{k}}{\partial z^2} = \frac{l_c}{\kappa_{\text{eff}}} 4F\overline{j}_e l_c - \frac{RT}{4F}\frac{\partial^2 \ln \overline{x}}{\partial z^2} \quad \text{[D-2]}$$

$$b\frac{\partial \ln \overline{k}}{\partial z}\bigg|_{z=0,c} = \frac{RT}{4F}\frac{\partial \ln(\overline{x})}{\partial z}\bigg|_{z=0,c} \quad \text{[D-3]}$$

$$b\frac{\partial \ln \overline{k}}{\partial z}\bigg|_{z=0,c} = -\frac{l_c}{\kappa_{\text{eff}}}\overline{I} \quad \text{[D-4]}$$

After combining Eq. 27 and Eq. B-9 to B-13 with Eq. D-1 to D-4, we can find that the $\overline{k}$ profile as well as the $\overline{x}$ profile is uniquely determined for the same steady-state operating current density, regardless of the change of $i_{\text{ref}}/(4Fc_{\text{ref}})$. To calculate the impedance response of an air cathode, we need to solve Eq. B-17 to B-28 and C-1 to C-2, which are directly related to the $\overline{k}$ profile instead of the value of $i_{\text{ref}}/(4Fc_{\text{ref}})$. With an unique $\overline{k}$ distribution in the cathode CAL for the same steady-state operating current density, we find that the impedance responses, Z_{Re} and Z_{Im}, of an air cathode are independent of the change of $i_{\text{ref}}/(4Fc_{\text{ref}})$. This conclusion is also valid for an O_2 cathode.

Further inspection of Fig. 9a reveals that the change of $i_{\text{ref}}/(4Fc_{\text{ref}})$ causes a translational movement of a polarization curve in the $\overline{\Phi}_1$ direction. The translational distance can be estimated by Eq. D-1.

List of Symbols

b Tafel slope, $b = 0.0261$ V
c concentration of the dissolved O_2 in the liquid phase, mol/cm^3
c_{ref} a reference concentration of the dissolved O_2 in the liquid phase, mol/cm^3
$\overline{c}$ steady-state concentration of the dissolved O_2 in the liquid phase, mol/cm^3
$\tilde{c}$ deviation amplitude of the concentration of the dissolved O_2 in the liquid phase, mol/cm^3
c_G total concentration of a gas flow, $c_G = P/(RT)$, mol/cm^3
C_{dl} double-layer capacitance of the Pt/carbon composite, F/cm^3
D diffusion coefficient of the dissolved O_2 in a free liquid stream, cm^2/s
D_{ON} binary diffusion coefficient of O_2-N_2 in the gas pores of a porous media, cm^2/s
D_{OW} binary diffusion coefficient of O_2-water vapor in the gas pores of a porous media, cm^2/s
D_{NW} binary diffusion coefficient of N_2-water vapor in the gas pores of a porous media, cm^2/s
E equilibrium potential of a cathode, V
E_O^0 standard equilibrium potential of an O_2 electrode in reference to a standard H_2 electrode (at the temperature of T and the O_2 partial pressure of 1.0 atm), V
f_p impedance peak frequency, Hz
F Faraday constant, 96,487 C/equiv.
H Henry's constant, [mol/cm^3(l)]/[mol/cm^3(g)]
I operating current density of the cathode, A/cm^2
I_F characteristic current density, A/cm^2
$\overline{I}$ steady-state operating current density of the cathode, A/cm^2
$\tilde{I}$ amplitude of the perturbation operating current density, A/cm^2
i_{ref} exchange current density of the O_2 reduction reaction per unit volume of the Pt/carbon composite evaluated at c_{ref}, A/cm^3
i_2 electrolyte current, A/cm^2
j imaginary sign, $\sqrt{-1}$
$4Fj_e$ reaction current per unit volume of the CAL, A/cm^3
$4F\overline{j}_e$ steady-state reaction current per unit volume of the CAL, A/cm^3
$4F\tilde{j}_e$ deviation amplitude of reaction current per unit volume of the CAL, A/cm^3
j_O accumulation rate of O_2 in the gas pores of the CAL, mol/cm^3/s
$\overline{j}_O$ steady-state accumulation rate of O_2 in the gas pores of the CAL, mol/cm^3/s
$\tilde{j}_O$ deviation amplitude of the accumulation rate of O_2 in the gas pores of the CAL, mol/cm^3/s
l_c thickness of the CAL, cm
l_B thickness of the GDL, cm
N_N N_2 flux, cm^2/s
N_O O_2 flux, cm^2/s
N_W water vapor flux, cm^2/s
P total gas pressure, atm
p Bruggeman coefficient, 0.5
R universal gas constant, 8.3143 J/mol/K
R_a radius of a spherical agglomerate particle, cm
r normalized spherical coordinate
T absolute cell temperature, K
U equilibrium potential of an O_2 electrode, V
x mole fraction of O_2 in the gas pores
$\overline{x}$ steady-state mole fraction of O_2 in the gas pores
$\tilde{x}$ deviation amplitude of the mole fraction of O_2 in the gas pores
y mole fraction of N_2
z normalized spatial coordinate in either the GDL or CAL, $0 \leqslant z \leqslant 1$

Greek

ε volume fraction of the liquid phase in an agglomerate particle
η overpotential, V
$\overline{\eta}$ steady state overpotential, V
$\tilde{\eta}$ deviation amplitude of the overpotential, V
φ_B volume fraction of gas pores in the GDL
φ_c volume fraction of gas pores in the CAL
κ_{eff} effective ionic conductivity of the electrolyte, S cm^{-1}
Φ_1 solid-phase potential, V
Φ_2 electrolyte potential, V

Subscripts

c CAL
B GDL
Re real part
Im imaginary part

References

1. T. E. Springer, M. S. Wilson, and S. Gottesfeld, *J. Electrochem. Soc.*, **140**, 3513 (1993).
2. D. M. Bernardi and M. W. Verbrugge, *J. Electrochem. Soc.*, **139**, 2477 (1992).
3. L. Pisani, G. Murgia, M. Valentini, and B. D. Aguanno, *J. Electrochem. Soc.*, **149**, A899 (2002).
4. F. Jaouen, G. Lindbergh, and G. Sundholm, *J. Electrochem. Soc.*, **149**, A437 (2002).
5. T. E. Springer and I. D. Raistrick, *J. Electrochem. Soc.*, **136**, 1594 (1989).
6. T. E. Springer, T. A. Zawodzinski, M. S. Wilson, and S. Gottesfeld, *J. Electrochem. Soc.*, **143**, 587 (1996).
7. T. E. Springer, in *Tutorials in Electrochemical Engineering*, R. F. Savinell, J. M. Fenton, A. West, S. L. Scanlon, and J. W. Weidner, Editors, Vol. 99-14, p. 208, The Electrochemical Society Proceedings Series, Pennington, NJ (1999).
8. R. B. Bird, W. E. Steward, and E. N. Lightfoot, *Transport Phenomena*, p. 570, John Wiley & Sons, New York (1960).
9. M. Doyle, J. P. Meyers, and J. Newman, *J. Electrochem. Soc.*, **147**, 99 (2000).
10. Q. Guo, M. Cayetano, Y. Tsou, E. S. De Castro, and R. E. White, *J. Electrochem. Soc.*, **150**, A1440 (2003).
11. J. S. Newman, *Electrochemical Systems*, 2nd ed., p. 460, Prentice Hall, Englewood Cliffs, NJ (1991).
12. G. J. Borse, *Fortran 77 and Numerical Methods for Engineers*, p. 504, PWS Engineering, Boston, MA (1985).
13. T. J. P. Freire and R. Gonzalez, *J. Electroanal. Chem.*, **503**, 57 (2001).
14. E. L. Cussler, *Diffusion Mass Transfer in Fluid Systems*, 2nd ed., p. 103, Cambridge University Press, New York (1997).
15. A. Parthasaranthy, S. Srinivasan, and A. J. Appleby, *J. Electrochem. Soc.*, **139**, 2530 (1992).